Inelastic scattering of transversely structured free electrons from nanophotonic targets: Theory and computation

Austin G. Nixon ⬡,[1] Matthieu Chalifour ⬡,[2] Marc R. Bourgeois ⬡,[1] Michael Sanchez,[2] and David J. Masiello ⬡[1,*]

[1]*Department of Chemistry, University of Washington, Seattle, Washington 98195, USA*
[2]*Department of Physics, University of Washington, Seattle, Washington 98195, USA*

Recent advancements in abilities to create and manipulate the electron's transverse wave function within the transmission electron microscope (TEM) and scanning TEM have enabled vectorially resolved electron-energy-loss (EEL) and -gain (EEG) measurements of nanoscale and quantum material responses using pre- and postselected free-electron states. This newfound capability is prompting renewed theoretical interest in quantum-mechanical treatments of inelastic-electron-scattering observables and the information they contain. Here we present a quantum-mechanical treatment of the inelastic scattering of free electrons between pre- and postselected transverse states with fully retarded electron-sample interactions for both spontaneous EEL and continuous-wave laser-stimulated EEG measurements. General expressions for the state-resolved energy-loss and -gain rates are recast in forms amenable to numerical calculation using the method of coupled dipoles. We numerically implement our theory within the electron-driven discrete dipole approximation code and use it to investigate specific examples that highlight its versatility regarding the number, size, geometry, and material composition of the target specimen as well as its ability to describe matter-wave diffraction from finite nanoscopic targets.

I. INTRODUCTION

Leveraging recent instrumental advancements in energy monochromation and aberration correction, inelastic scattering of free electrons has become an effective technique to spectroscopically characterize and image atomic and molecular [1–3], biological [4–6], solid-state [7–11], and nanophotonic [12,13] systems with unprecedented spatial resolution. Simultaneously, optical spectroscopies and microscopies based upon the absorption, scattering, extinction, and emission of electromagnetic waves continue to be indispensable tools used to probe the same systems, albeit with spatial resolution limitations imposed by the optical diffraction limit. Light-based spectromicroscopies can often be enhanced by taking advantage of optical selection rules stemming from the intrinsic linear and spin angular momentum degrees of freedom of the photon [14]. In addition to the polarization degrees of freedom arising from the intrinsic spin angular momentum, photons can also be prepared in specific orbital angular momentum (OAM) states defined by the azimuthal phase $e^{i\ell\phi}$ [15]. Due to the helical nature of their spiraling phase fronts, light beams characterized by such a quantized topological charge ℓ are commonly referred to as optical vortex or twisted light beams [16,17]. Motivated in part by the infinite-dimensional Hilbert space offered by the OAM basis [18], the ability to prepare [19], sort [20], and measure [21] these optical OAM states has driven applications in quantum information science using photons with quantized azimuthal

and radial labels [17,22–26]. Moreover, transverse sculpting of the radiation field in general has lead to the development of new gauge transformations, such as the twisted light gauge [27,28], construction of free-space optical skyrmionic beams [29], excitations of forbidden transitions in atomic isotopes [30], and the use of vortex γ-ray photons to selectively probe high-energy resonances in photonuclear reactions [31].

Unlike photons, electrons prepared and measured in currently available transmission electron microsopes (TEMs), scanning TEMs (STEMs), or ultrafast TEMs are accurately described by the spinless free-particle Schrödinger equation and consequently lack intrinsic polarization degrees of freedom [17]. Despite this limitation, linear-momentum-based selection rules based on quantum-mechanical treatments of the inelastic-scattering process have been long understood and exploited in core-loss electron-energy-loss (EEL) spectroscopy [32–35] and have enabled measurements of magnetic circular dichroism [36–41], characterization of site-specific defects in atomic crystals [42], and visualization of the electromagnetic fields of atomic-scale systems [43]. Inspired by the creation and manipulation of optical vortex states, development of techniques for shaping the transverse phase profile [44] and OAM content of free electrons via holographic masks [45–47], spiral phase plates [48], and shaped laser pulses [49,50] has been at the forefront of low-loss EEL spectroscopy (less than approximately 50 eV) [51]. Furthermore, borrowing ideas from quantum optics, the preparation of free-electron qubits carrying information in the form of quantized energy or OAM states using laser pulses [52–54], holographic masks, or spiral phase plates [55–57] has driven the continued development of free electrons as holders and

*masiello@uw.edu

propagators of quantum information. In parallel, the ability to generate phase-structured incident electron states and sort them based upon their OAM content [58] has fueled numerous investigations of inelastic electron scattering between states with pre- and postselected transverse phase profiles in the low-loss regime [59–68].

In this paper, we expound upon a recently introduced theoretical framework describing the fully retarded inelastic scattering of phase-shaped free-electron beams in the electron microscope [67]. Specifically, with emphasis placed on the low-loss regime, we investigate the theory of transversely phase-shaped EEL spectroscopy in both narrow-beam and wide-field limits and laser-stimulated electron-energy-gain (EEG) spectroscopy in the narrow-beam limit. Section II presents a derivation of the energy-resolved inelastic-electron-scattering rate, including both EEL and EEG processes. Transversely structured free-electron states that can be prepared within currently available TEMs and STEMs are subsequently reviewed in Sec. III. Section IV introduces the transition current density associated with transitions between such states. Expressions for EEL and EEG observables are derived in Sec. V for both wide-field and focused electron beams, including those with nonuniform transverse phase structure, such as twisted electron beams. Numerical implementation of the presented inelastic-electron-scattering theory based on the method of coupled dipoles is described in Sec. VI, including EEL and EEG probabilities and the EEL double-differential scattering cross section (DDCS). Numerical calculations are presented for prototypical nanophotonic systems, underscoring particular advantages of our numerical approach, including its (i) flexibility regarding target size, shape, composition, and number, (ii) facile extension to accommodate arbitrary initial and final free-electron transverse states, and (iii) ability to capture signatures of matter-wave diffraction and interference arising from scattering from individual and multiple nanoscale targets. Gaussian units are used throughout.

II. INELASTIC-FREE-ELECTRON SCATTERING: STATE- AND ENERGY-RESOLVED EEL AND EEG RATES

Here we review the retarded theory of inelastic electron scattering for the calculation of EEL and laser-stimulated EEG processes [51,66,67,69–74]. The target material is described through its bound electromagnetic responses characterized by dielectric function $\xi(\omega)$, while the electron probe is examined for both delocalized and localized electron wave functions. The light-matter potential governing such interactions takes the form

$$\hat{V} = \frac{e}{2mc}(\hat{\mathbf{A}} \cdot \hat{\mathbf{p}} + \hat{\mathbf{p}} \cdot \hat{\mathbf{A}}) \quad (1)$$

under minimal coupling in the generalized Coulomb gauge [75] $\nabla \cdot \xi(\mathbf{x})\hat{\mathbf{A}}(\mathbf{x}, t) = 0$, where the $\hat{\rho}\hat{\Phi}$ term makes no contribution in the absence of free charges describing the target. The probing electron's charge and mass are $-e$ and m, respectively, and c is the speed of light in vacuum; $\hat{\mathbf{A}}$ and $\hat{\mathbf{p}}$ are quantum-mechanical operators for the vector potential of the target and linear momentum of the free-electron probe, respectively. Owing to the inherently weak nature of electron-photon coupling, the inelastic-scattering probability can be obtained using first-order time-dependent perturbation theory.
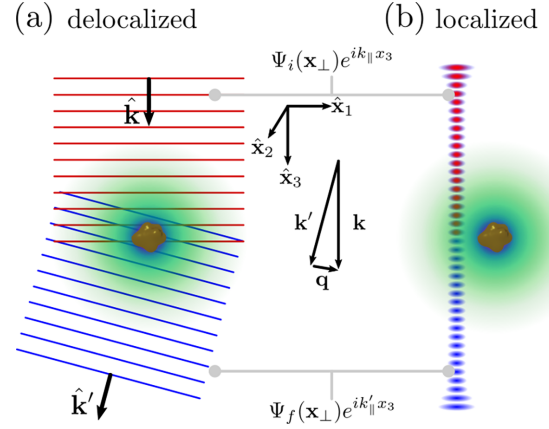
FIG. 1. Scheme showing the inelastic scattering of transversely (a) delocalized and (b) localized free electrons with wave functions of the separable form $\Psi(\mathbf{x}_\perp)e^{ik_\parallel x_3}$. (a) Initial electron plane wave (red) with wave vector $\mathbf{k} = (\mathbf{k}_\perp, k_\parallel)$ interacting with the vector potential (shaded green) of a target specimen. Following the interaction, the electron is postselected for the plane-wave state $\mathbf{k}' = (\mathbf{k}'_\perp, k'_\parallel)$ (blue). The momentum recoil wave vector associated with this transition is $\mathbf{q} = \mathbf{k} - \mathbf{k}'$. (b) Transversely localized electron beam with preselected transverse wave function $\Psi_i(\mathbf{x}_\perp)$ (red) interacting with the same target and postselected in $\Psi_f(\mathbf{x}_\perp)$ (blue).

The transition rate describing the scattering of an electron from initial state $|\psi_i\rangle$ to final state $|\psi_f\rangle$ while simultaneously exciting or deexciting the target from initial state $|\Phi_\nu\rangle$ to final state $|\Phi_{\nu'}\rangle$ is given by

$$w_{fi} = \frac{2\pi}{\hbar} \sum_{\nu\nu'} |\langle\Phi_{\nu'}|\langle\psi_f|\hat{V}|\psi_i\rangle|\Phi_\nu\rangle|^2 \delta(E_f - E_i), \quad (2)$$

where $E_i = \hbar\varepsilon_i + \hbar\omega_\nu$ and $E_f = \hbar\varepsilon_f + \hbar\omega_{\nu'}$ are the initial and final energies of the composite system, respectively, $\hbar\varepsilon_{i\,(f)} = \gamma_{i\,(f)}mc^2$ represents the initial (final) energy of the probing electron, and $\gamma_{i\,(f)} = [1 - (v_{i\,(f)}/c)^2]^{-1/2}$ is the initial (final) Lorentz contraction factor. Section III details specific TEM and STEM electron states, including those that are phase shaped transversely to their propagation direction (see Fig. 1), but for now we remain agnostic to their identity. After some algebra, the transition matrix elements of the scattering potential in Eq. (1) can be expressed as

$$V_{\nu'f\nu i}(t) = \langle\Phi_{\nu'}|\langle\psi_f|\hat{V}(t)|\psi_i\rangle|\Phi_\nu\rangle$$
$$= \langle\Phi_{\nu'}| - \frac{1}{c}\int d\mathbf{x}\,\mathbf{A}(\mathbf{x}, t) \cdot \mathbf{J}_{fi}(\mathbf{x}, t)|\Phi_\nu\rangle, \quad (3)$$

where $\mathbf{J}_{fi}(\mathbf{x}, t) = \mathbf{J}_{fi}(\mathbf{x})e^{-i(\varepsilon_i - \varepsilon_f)t}$ is the transition current density [67] with

$$\mathbf{J}_{fi}(\mathbf{x}) = \frac{i\hbar e}{2m}[\psi_f^*(\mathbf{x})\nabla\psi_i(\mathbf{x}) - \psi_i(\mathbf{x})\nabla\psi_f^*(\mathbf{x})] \quad (4)$$

defined in terms of the probe scattering states $\psi_i(\mathbf{x}, t) = \psi_i(\mathbf{x})e^{-i\varepsilon_i t}$ and $\psi_f(\mathbf{x}, t) = \psi_f(\mathbf{x})e^{-i\varepsilon_f t}$. By continuity, i.e., $\nabla \cdot \mathbf{J}_{fi}(\mathbf{x}, t) = -\dot{\rho}_{fi}(\mathbf{x}, t)$, $\mathbf{J}_{fi}(\mathbf{x}, t)$ is connected to the transition charge density $\rho_{fi}(\mathbf{x}, t) = -e\psi_f^*(\mathbf{x}, t)\psi_i(\mathbf{x}, t)$.

Both the EEL and EEG scattering rates derive from Eq. (3) but involve different vector potentials of distinct physical origin. In the case of EEL, solving the

vector Helmholtz equation on the domain of the target produces a set of eigenmode functions $\mathbf{f}_\nu(\mathbf{x})$ and associated eigenmode frequencies ω_ν,[1] which serve as a basis to expand the target vector potential [75]. In terms of this set $\{\mathbf{f}_\nu(\mathbf{x})\}_\nu$, $\mathbf{A}(\mathbf{x}, t) = \sum_\nu [\mathbf{A}_\nu^{(+)}(\mathbf{x}) a_\nu e^{-i\omega_\nu t} + \mathbf{A}_\nu^{(-)}(\mathbf{x}) a_\nu^\dagger e^{i\omega_\nu t}]$, with $\mathbf{A}_\nu^{(+)}(\mathbf{x}) = c\sqrt{2\pi\hbar/\omega_\nu}\mathbf{f}_\nu(\mathbf{x})$, $\mathbf{A}_\nu^{(-)}(\mathbf{x}) = c\sqrt{2\pi\hbar/\omega_\nu}\mathbf{f}_\nu^*(\mathbf{x})$, and $[\mathbf{A}_\nu^{(+)}]^\dagger = \mathbf{A}_\nu^{(-)}$, where $a_\nu^\dagger$ (a_ν) is the creation (annihilation) operator responsible for inducing optical excitations (de-excitations) in the νth target mode. In the case of EEG, the target vector potential can still be expanded onto the $\{\mathbf{f}_\nu(\mathbf{x})\}_\nu$ basis; however, it is the response vector potential induced by a stimulating laser field. In either case, Eq. (3) becomes

$$
V_{\nu'f\nu i}(t) = -\frac{1}{c}\left(\sqrt{n_\nu}\delta_{\nu',\nu-1}\int d\mathbf{x}\, \mathbf{A}_\nu^{(+)}(\mathbf{x})\cdot\mathbf{J}_{fi}(\mathbf{x})e^{-i\omega_\nu t}\right.
$$
$$
\left. + \sqrt{n_\nu+1}\,\delta_{\nu',\nu+1}\int d\mathbf{x}\, \mathbf{A}_\nu^{(-)}(\mathbf{x})\cdot\mathbf{J}_{fi}(\mathbf{x})e^{i\omega_\nu t}\right)
$$
$$
\times\, e^{-i(\varepsilon_i-\varepsilon_f)t}, \tag{5}
$$

where n_ν is the occupancy of the νth target mode. When carrying out the derivations of inelastic-electron-scattering processes, the first and second terms in Eq. (5) correspond to EEG and EEL events, respectively. The energy-conserving δ function in Eq. (2), when written in the equivalent forms

$$
\delta(E_f-E_i) = \frac{1}{\hbar}\int d\omega \times \begin{cases} \delta(\omega-\varepsilon_{if})\delta(\omega-\omega_{\nu'\nu}) & \text{(EEL)} \\ \delta(\omega+\varepsilon_{if})\delta(\omega-\omega_{\nu\nu'}) & \text{(EEG)}, \end{cases} \tag{6}
$$

with $\varepsilon_{if} = \varepsilon_i - \varepsilon_f$ and $\omega_{\nu\nu'} = \omega_\nu - \omega_{\nu'}$, will aid in this connection to EEL and EEG.

In EEL events, the probing electron may transfer energy to and retrieve energy from any of the target modes which must be summed over to account for all such loss processes where the electron acts as both pump and probe. After summing over target states ν and ν', the EEL scattering rate becomes

$$
w_{fi}^{\text{loss}} = \frac{2\pi}{\hbar c^2}\sum_\nu\int d\mathbf{x}\, d\mathbf{x}'\mathbf{J}_{fi}^*(\mathbf{x})\cdot\mathbf{A}_\nu^{(+)}(\mathbf{x})\mathbf{A}_\nu^{(-)}(\mathbf{x}')\cdot\mathbf{J}_{fi}(\mathbf{x}')
$$
$$
\times\,\delta(E_f-E_i), \tag{7}
$$

while in the case of EEG the stimulating laser field is taken to populate the specific target state ν, leaving only a sum over final target states ν' to be performed, resulting in

$$
w_{fi}^{\text{gain}} = \frac{2\pi}{\hbar c^2}\int d\mathbf{x}\, d\mathbf{x}'\mathbf{J}_{fi}^*(\mathbf{x})\cdot\mathbf{A}_\nu^{(-)}(\mathbf{x})\mathbf{A}_\nu^{(+)}(\mathbf{x}')\cdot\mathbf{J}_{fi}(\mathbf{x}')
$$
$$
\times\,\delta(E_f-E_i). \tag{8}
$$

Again note that the target vector potentials $\mathbf{A}_\nu^{(\pm)}(\mathbf{x})$ in the EEG rate in Eq. (8) are understood to originate in response to external laser stimulation and are not induced by the probing electron's transition current $\mathbf{J}_{fi}(\mathbf{x})$.

---

[1]As presented, the eigenmode expansion of the vector potential is rigorously correct only for lossless dielectric cavities. Losses can be incorporated from the outset by instead expanding the vector potential onto the basis of quasinormal modes [76–78]. The resulting EEL rate expressions exhibit equivalent dependence on the Green's dyadic irrespective of the presence or absence of losses.

From Eqs. (6) and (7), together with the relationship $w_{fi} = \int d\omega\, w_{fi}(\omega)$, the frequency-resolved EEL rate $w_{fi}^{\text{loss}}(\omega)$ can be derived. By expressing the target vector potential in terms of mode functions, i.e., $\mathbf{A}_\nu^{(+)}(\mathbf{x})\mathbf{A}_\nu^{(-)}(\mathbf{x}') = (2\pi\hbar c^2/\omega_\nu)\mathbf{f}_\nu(\mathbf{x})\mathbf{f}_\nu^*(\mathbf{x}')$, Eq. (7) can be written in terms of the target's electromagnetic Green's tensor $\overset{\leftrightarrow}{\mathbf{G}}(\mathbf{x},\mathbf{x}',\omega) = \sum_\nu \mathbf{f}_\nu(\mathbf{x})\mathbf{f}_\nu^*(\mathbf{x}')/(\omega^2-\omega_\nu^2+i0^+)$. More specifically, the EEL rate is formulated in terms of the imaginary part of the Green's dyadic $\text{Im}\{\overset{\leftrightarrow}{\mathbf{G}}(\mathbf{x},\mathbf{x}',\omega)\} = -\sum_\nu(\pi/2\omega_\nu)\mathbf{f}_\nu(\mathbf{x})\mathbf{f}_\nu^*(\mathbf{x}')\delta(\omega-\omega_{\nu'\nu})$. As a result, the state- and frequency-resolved EEL transition rate then becomes

$$
w_{fi}^{\text{loss}}(\omega) = -\frac{8\pi}{\hbar}\int d\mathbf{x}\, d\mathbf{x}'\mathbf{J}_{fi}^*(\mathbf{x})\cdot\text{Im}[\overset{\leftrightarrow}{\mathbf{G}}(\mathbf{x},\mathbf{x}',\omega)]\cdot\mathbf{J}_{fi}(\mathbf{x}')
$$
$$
\times\,\delta(\omega-\varepsilon_{if})
$$
$$
= -\frac{8\pi}{\hbar}\int d\mathbf{x}\, d\mathbf{x}'\text{Im}[\mathbf{J}_{fi}^*(\mathbf{x})\cdot\overset{\leftrightarrow}{\mathbf{G}}(\mathbf{x},\mathbf{x}',\omega)\cdot\mathbf{J}_{fi}(\mathbf{x}')]
$$
$$
\times\,\delta(\omega-\varepsilon_{if}), \tag{9}
$$

where the bottom line holds for reciprocal media characterized by $\overset{\leftrightarrow}{\mathbf{G}}(\mathbf{x},\mathbf{x}',\omega) = \overset{\leftrightarrow}{\mathbf{G}}^T(\mathbf{x}',\mathbf{x},\omega)$. Note that for general phase-shaped EEL processes described by Eq. (9), the transition current density can point arbitrarily in three-dimensional (3D) space and is not restricted to lie along the TEM axis.

Alternatively, for the case of laser-stimulated EEG, Eqs. (6) and (8) determine the frequency-resolved EEG rate. The positive (negative)-frequency portion of the target's laser-induced response field can be expressed in terms of its induced vector potential as $\mathbf{E}_\nu^{(\pm)}(\mathbf{x}) = (\pm i\omega_\nu/c)\mathbf{A}_\nu^{(\pm)}(\mathbf{x})$. When the stimulating laser excites a coherent state of the target $|\alpha_\nu\rangle$, the frequency-resolved EEG rate

$$
w_{fi}^{\text{gain}}(\omega) = 2\pi\left(\frac{|\alpha_\nu|}{\hbar\omega_\nu}\right)^2\left|\int d\mathbf{x}\, \mathbf{E}_\nu^{(+)}(\mathbf{x})\cdot\mathbf{J}_{fi}(\mathbf{x})\right|^2
$$
$$
\times\,\delta(\omega+\varepsilon_{if})\delta(\omega-\omega_{\nu\nu'}) \tag{10}
$$

is proportional to the volume integral of the 3D vector transition current density $\mathbf{J}_{fi}(\mathbf{x})$ projected onto the laser-induced electric field $\mathbf{E}_\nu^{(+)}(\mathbf{x})$ of the target. For simplicity, the applied monochromatic continuous-wave laser field is chosen to couple to the target's νth excited state only. In the low-photon-occupancy limit ($|\alpha_\nu| \approx 1$), this coherent-state description yields

$$
w_{fi}^{\text{gain}}(\omega) = 2\pi\left(\frac{1}{\hbar\omega_\nu}\right)^2\left|\int d\mathbf{x}\, \mathbf{E}_\nu^{(+)}(\mathbf{x})\cdot\mathbf{J}_{fi}(\mathbf{x})\right|^2
$$
$$
\times\,\delta(\omega+\varepsilon_{if})\delta(\omega-\omega_{\nu\nu'}), \tag{11}
$$

which has been stated previously [66]. As will be shown in Sec. V A, if the appropriate choices for the initial and final electron states are made, Eqs. (9) and (11) reduce to the conventional EEL and EEG probabilities found in the literature [51,66,70,71] but, as expressed here, are generalized to potentially describe polarized EEL and EEG measurements where the wave function of the probing electron is phase structured in the plane orthogonal to its motion. Therefore, the approach producing Eqs. (9)–(11) casts phase-shaped EEL and EEG interactions both within the same framework and on equal footing.
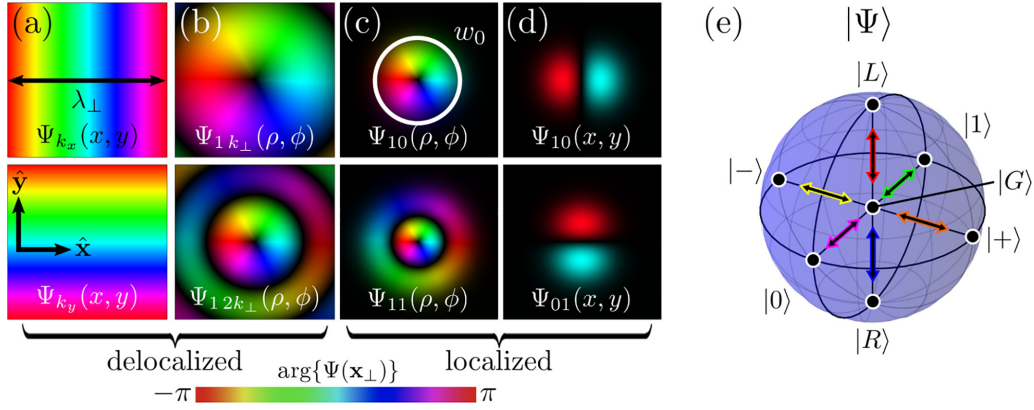
FIG. 2. Transverse free-electron states. Wave functions $\Psi(x, y)$ are visualized in the $z = 0$ plane with position-dependent phase indicated by the color of the respective intensity profiles. Black represents low wave-function density. (a) Plane-wave states with $\mathbf{k}_\perp$ along $\hat{\mathbf{x}}$ (top) and $\hat{\mathbf{y}}$ (bottom). (b) Bessel beam states $\Psi_{\ell k_\perp}(\rho, \phi)$ with $\ell = 1$ and radial wave number $k_\perp$ (top) and $2k_\perp$ (bottom). (c) LG states $\Psi_{\ell p}(\rho, \phi)$ with $\ell = 1$ and $p = 0$ (top) and $p = 1$ (bottom). (d) HG states $\Psi_{nm}(x, y)$ with $n = 1$ and $m = 0$ (top) and $n = 0$ and $m = 1$ (bottom). (e) In the $\ell = \pm 1$ OAM subspace, the first-order LG states $|L/R\rangle$ can be used as basis states spanning the Bloch sphere with antipodal points $\{|0\rangle, |1\rangle\}$, $\{|+\rangle, |-\rangle\}$, and $\{|L\rangle, |R\rangle\}$; states with constant spatial phase are defined as $|G\rangle$ and placed at the sphere center. Colored arrows represent transitions between $|G\rangle$ and the states at the labeled antipodal points.

III. TRANSVERSELY PHASE-STRUCTURED FREE-ELECTRON STATES

This section introduces various spinless free-electron states relevant to the forthcoming discussion of phase-structured EEL and EEG measurements in TEM and STEM instruments. The states are (i) energy eigenstates and thereby separable into spatial and temporal parts as $\psi(\mathbf{x}, t) = \psi(\mathbf{x})e^{-i\varepsilon t}$ and (ii) separable within an orthogonal coordinate system $\mathbf{x} = (x_1, x_2, x_3)$ into transverse and longitudinal functions $\psi(\mathbf{x}) = \Psi(x_1, x_2)e^{ik_\parallel x_3}$. The electron wave functions are translationally invariant along the TEM axis, defined as $x_3 \equiv z$. Transversely delocalized states are investigated first, beginning with plane-wave and vortex-Bessel-beam states originating as separable solutions in the Cartesian and cylindrical coordinate systems, respectively. Subsequently, transversely localized and nondiffracting wave functions, including Hermite-Gauss (HG) and twisted electron Laguerre-Gauss (LG) states, are presented.

Plane-wave solutions are separable in Cartesian coordinates with well-defined linear momentum $\mathbf{p} = \hbar\mathbf{k}$. The spatial wave function describing a free electron in the 3D Cartesian space $\mathbf{x} = (x, y, z)$ is

$$\psi_{\mathbf{k}}(x, y, z) = \left(\frac{1}{\sqrt{L}}\right)^3 e^{i\mathbf{k}\cdot\mathbf{x}}, \tag{12}$$

where $\mathbf{k} = (\mathbf{k}_\perp, k_\parallel)$ is the wave vector and L is the box quantization length. Phase plots of two transverse plane-wave states $\Psi_{k_x}(x, y)$ and $\Psi_{k_y}(x, y)$, with orthogonal wave vectors $\mathbf{k}_\perp = k_x\hat{\mathbf{x}}$ and $\mathbf{k}_\perp = k_y\hat{\mathbf{y}}$ and corresponding transverse wavelengths $\lambda_{\perp x} = 2\pi/k_x$ and $\lambda_{\perp y} = 2\pi/k_y$, are displayed in the top and bottom panels of Fig. 2(a) for $\lambda_{\perp x} = \lambda_{\perp y} = \lambda_\perp$, respectively. Electrons can also be prepared in coherent superposition states, with one example of such a state being $\psi_{k_x k_y}^\chi(x, y, z) = L^{-3/2}(e^{ik_x x} + e^{ik_y y}e^{i\chi})e^{ik_\parallel z}/\sqrt{2}$, where the relative phase χ between the two orthogonal electron wave-vector components k_x and k_y can take values $0 \leqslant \chi \leqslant 2\pi$ [36–38].

When expressed in the cylindrical coordinate system defined by $\mathbf{x} = (\rho, \phi, z)$, the separable solutions are nondiffracting Bessel waves of the form [79–82]

$$\psi_{\ell k_\perp}(\rho, \phi, z) \propto J_{|\ell|}(k_\perp \rho)e^{i\ell\phi}e^{ik_\parallel z}. \tag{13}$$

Here $J_{|\ell|}(k_\perp \rho)$ are Bessel functions of the first kind, ℓ is the azimuthal quantum number of the cylindrically symmetric state, $k_\perp$ is the radial wave-vector component, and $k_\parallel$ is the longitudinal wave-vector component [83]. Such states are eigenstates of the z component of the OAM operator $\hat{L}_z = -i\hbar\partial/\partial\phi$ with eigenvalue $\ell\hbar$. Specific examples of Bessel states are shown in Fig. 2(b) for two different values of $k_\perp$.

Transversely localized free-electron states can be constructed within the paraxial approximation to the Schrödinger equation, where the electron momentum along the TEM axis is much greater than its transverse momentum, i.e., $k_\perp \ll |\mathbf{k}|$. Since they are eigenstates of the $\hat{L}_z$ operator, LG states carry a quantized azimuthal component ℓ. In the nondiffracting, i.e., collimated, limit defined by the infinite Rayleigh range, the LG wave functions have the form of quantized Landau states [79,83] given by

$$\psi_{\ell p}(\rho, \phi, z) = \frac{(\sqrt{2}\rho/w_0)^{|\ell|}}{w_0\sqrt{L}}\sqrt{\frac{2p!}{\pi(|\ell| + p)!}}L_p^{|\ell|}\left(\frac{2\rho^2}{w_0^2}\right)$$
$$\times e^{-\rho^2/w_0^2}e^{i\ell\phi}e^{ik_\parallel z}, \tag{14}$$

where $L_p^{|\ell|}$ are the Laguerre polynomials, with ℓ and p the azimuthal and radial quantum numbers, respectively, and w_0 is the z-independent beam waist. Figure 2(c) displays two different LG modes with finite beam waists w_0.

Similarly, the HG family of transversely localized wave functions are solutions to the paraxial wave equation in the Cartesian coordinate system. Since the nondiffracting LG and HG states each comprise a complete orthonormal basis, any LG (HG) state can be synthesized from the appropriate coherent superposition of HG (LG) states [84]. Unlike the LG transverse states, the HG states lack a well-defined azimuthal

phase and, owing to the fact that they are not eigenstates $\hat{L}_z$, do not carry a single OAM unit of ℓ. In the nondiffracting limit, the HG states take the form

$$\psi_{nm}(x, y, z) = \frac{2^{-(n+m)/2}}{w_0 \sqrt{L}} \sqrt{\frac{2}{\pi n! m!}} H_n\left(\frac{x\sqrt{2}}{w_0}\right) H_m\left(\frac{y\sqrt{2}}{w_0}\right)$$
$$\times \, e^{-(x^2+y^2)/w_0^2} e^{ik_\parallel z} \qquad (15)$$

and are labeled by the indices n and m, corresponding to the order of the x- and y-dependent Hermite polynomials H_n and H_m, respectively. Figure 2(d) displays the first-order x- and y-oriented HG modes with beam waists w_0, in contrast to the corresponding delocalized $\Psi_{k_x}(x, y)$ and $\Psi_{k_y}(x, y)$ plane waves displayed in Fig. 2(a).

Mirroring applications of optical OAM states, free electrons with quantized transverse degrees of freedom have recently been recognized as potential carriers of quantum information, specifically as free-electron OAM qubits. Realization of such OAM qubits has been made possible via holographic masks and spiral phase plates [45–48] or through tailored light sources [49,50]. Stemming from the separability of the electron wave function following condition (ii), the orthogonal transverse degrees of freedom can be used as orthonormal basis states $|0\rangle$ and $|1\rangle$ on the Bloch sphere [Fig. 2(e)]. Known as the horizontal and vertical basis states, respectively, linear combinations of $|0\rangle$ and $|1\rangle$ assemble the remaining antipodal points $|L/R\rangle = (1/\sqrt{2})(|0\rangle \pm i|1\rangle)$ and $|\pm\rangle = (1/\sqrt{2})(|0\rangle \pm |1\rangle)$. One example is the first-order LG states $\Psi_{\pm 10}(\rho, \phi) = \langle x_1 x_2 | L/R\rangle$ which span the truncated $\ell = \pm 1$ two-dimensional Hilbert space [56,57,84] and lie on the north and south poles of the Bloch sphere. Owing to the fact that $\Psi_{\pm 10}(\rho, \phi)$ can be expressed as linear combinations of the first-order HG states [15], $\Psi_{10}(x, y) = \langle x_1 x_2 | 0\rangle$ and $\Psi_{01}(x, y) = \langle x_1 x_2 | 1\rangle$ are the wave functions associated with the vertical and horizontal basis states, respectively. At the center of the Bloch sphere lies the Gaussian mode $\Psi_{00}(x, y) = \Psi_{00}(\rho, \phi) = \langle x_1 x_2 | G\rangle = \sqrt{2/\pi w_0^2} e^{-(x^2+y^2)/w_0^2} = \sqrt{2/\pi w_0^2} e^{-\rho^2/w_0^2}$. More generally, higher-order electron-vortex states with topological charge of $\pm \ell$ can be used to construct Bloch spheres for ℓ values other than unity [18]. Following the work of Ref. [67], under the appropriate limits, certain superpositions of electron plane-wave states can likewise be mapped onto points on the Bloch sphere [Fig. 2(e)]. In this scenario, the horizontal and vertical plane-wave wave functions $\Psi_{k_x}(x, y) = \langle x_1 x_2 | 0\rangle$ and $\Psi_{k_y}(x, y) = \langle x_1 x_2 | 1\rangle$ can be used to construct the north and south antipodal point wave functions $\Psi_{k_x k_y}^{\pm \pi/2}(x, y)$. Specifically, $\Psi_{k_x k_y}^{\pm \pi/2}(x, y) = \langle x_1 x_2 | L/R\rangle = (1/\sqrt{2})$ $[\Psi_{k_x}(x, y) + \Psi_{k_y}(x, y) e^{i\chi}]$ with $\chi = \pm \pi/2$. Located at the center of the Bloch sphere is the electron plane wave $\Psi_{k_\parallel}(x, y) = \langle x_1 x_2 | G\rangle = 1/L$ with spatially uniform transverse phase and purely longitudinal wave vector $\mathbf{k} = k_\parallel \hat{\mathbf{z}}$. As will be shown in the following section, transitions between OAM or linear momentum electron states residing on the Bloch sphere produce transition current densities with unique vector and phase profiles.

IV. TRANSITION CURRENT DENSITY

Here the transition current density $\mathbf{J}_{fi}(\mathbf{x})$ defined in Eq. (4) is examined for selected transitions between electron states introduced in the preceding section. This section begins with a summary of general properties of $\mathbf{J}_{fi}(\mathbf{x})$ that arise from the restrictions imposed on the forms of the wave functions and then highlights several general and specific forms of the transition current density for transitions involving delocalized and localized electron states. Note the following, regarding the arguments of the transition current density: Recall that the origin of time dependence in $\mathbf{J}_{fi}(\mathbf{x}, t) = \mathbf{J}_{fi}(\mathbf{x}) e^{i\varepsilon_{fi} t}$ as seen in Eq. (3) is a consequence of condition (i) imposed upon the electron wave functions introduced in the first paragraph of Sec. III. Therefore, as a matter of convenience and unless stated otherwise, we work with the time-independent version of the transition current density. In addition, when discussing the transition current density for Bessel, LG, and HG free-electron states, the subscripts of $\mathbf{J}_{fi}(\mathbf{x})$ refer explicitly to the final and initial transverse electron states. Figures 3(a) and 3(b) present LG and Bessel beam transitions, respectively, Fig. 3(c) involves transitions between plane-wave states, and Figs. 3(d) and 3(e) showcase the transition current density using focused first-order HG states.

Stemming from conditions (i) and (ii) required of the electron wave functions as stipulated in Sec. III, the transition current density given by Eq. (4) can be reexpressed as the sum of longitudinal ($\parallel$) and transverse ($\perp$) contributions, defined relative to the TEM axis, according to

$$\mathbf{J}_{fi}(\mathbf{x}) = \mathbf{J}_{fi}(\mathbf{x}_\perp) e^{iq_\parallel z} = [\mathbf{J}_{fi}^\perp(\mathbf{x}_\perp) + J_{fi}^\parallel(\mathbf{x}_\perp)\hat{\mathbf{z}}] e^{iq_\parallel z}. \qquad (16)$$

Explicitly, these components are

$$\mathbf{J}_{fi}^\perp(\mathbf{x}_\perp) = \frac{i\hbar e}{2mL} [\Psi_f^*(\mathbf{x}_\perp)\nabla_\perp \Psi_i(\mathbf{x}_\perp) - \Psi_i(\mathbf{x}_\perp)\nabla_\perp \Psi_f^*(\mathbf{x}_\perp)],$$

$$J_{fi}^\parallel(\mathbf{x}_\perp) = -\frac{\hbar e}{2mL} Q_\parallel \Psi_f^*(\mathbf{x}_\perp)\Psi_i(\mathbf{x}_\perp), \qquad (17)$$

where $Q_\parallel = k_\parallel + k_\parallel'$. It can be seen from the perpendicular component of Eq. (17) that interchange of the initial and final transverse states is equivalent to conjugation of the reciprocal scattering process, i.e., $\mathbf{J}_{if}(\mathbf{x}) = \mathbf{J}_{fi}^*(\mathbf{x})$.

A. Plane-wave states

First we consider transitions between individual incoming $\psi_{\mathbf{k}_i}(x, y, z)$ and outgoing $\psi_{\mathbf{k}_f}(x, y, z)$ plane-wave states of the probe, defined in Eq. (12), such that $\hbar \mathbf{q} = \hbar(\mathbf{k}_i - \mathbf{k}_f)$ is the momentum recoil associated with the transition. The transition current density associated with this case is

$$\mathbf{J}_{\mathbf{k}_f \mathbf{k}_i}(x, y, z) = -\frac{e\hbar}{2mL^3}(2\mathbf{k}_i - \mathbf{q}) e^{i\mathbf{q} \cdot \mathbf{x}}. \qquad (18)$$

Inspection of Eq. (18) reveals that the transverse component of the transition current density is directly proportional to the transverse recoil momentum, i.e., $\mathbf{J}_{\mathbf{k}_f \mathbf{k}_i}^\perp(x, y, z) \propto \mathbf{q}_\perp$. The phase and vector structure of the transition current density for an initial plane-wave state with transverse wave vector $\mathbf{k}_\perp = k_x \hat{\mathbf{x}}$ transitioning to the outgoing plane-wave state $\psi_{k_\parallel'}(x, y, z) = L^{-3/2} e^{ik_\parallel' z}$ is shown in the top panel of Fig. 3(c).
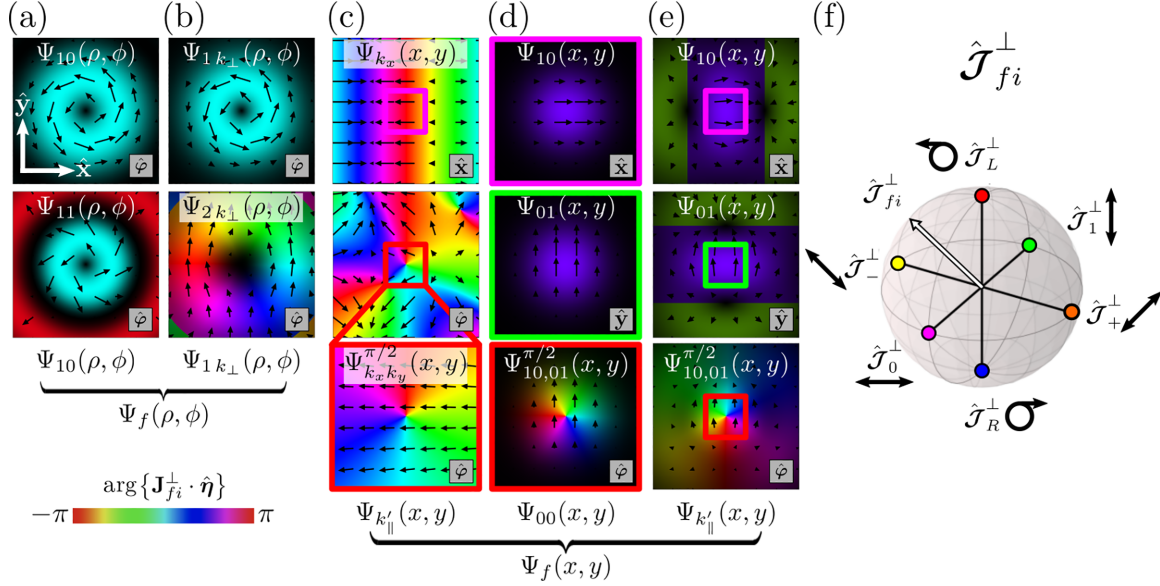
FIG. 3. Transition current density vector fields $\mathbf{J}_{fi}(\mathbf{x})$ in the $z = 0$ plane. The arrows within each panel show the direction and strength of the transverse component $\mathbf{J}_{fi}^{\perp}(\mathbf{x})$, while the underlying colormap indicates the phase $\mathbf{J}_{fi}^{\perp}(\mathbf{x}) \cdot \hat{\boldsymbol{\eta}}$ and intensity $|\mathbf{J}_{fi}^{\perp}(\mathbf{x})|$. The $\hat{\boldsymbol{\eta}}$ is displayed in the bottom right-hand corner of each panel. The initial transverse wave functions for the transition current density vector fields are labeled in the center at the top of each panel, while the final state is shown at the bottom of each column. (a) Transition current densities involving LG $\Psi_{\ell p}(\rho, \phi)$ initial and final states. The top panel shows the case of $\Psi_{10}(\rho, \phi) \rightarrow \Psi_{10}(\rho, \phi)$ with no transverse transition; the $\Psi_{11}(\rho, \phi) \rightarrow \Psi_{10}(\rho, \phi)$ transition in the bottom panel involves a transition in radial, but not OAM, quantum numbers. (b) Transitions between Bessel states $\Psi_{\ell k_{\perp}}(\rho, \phi)$. The top panel shows the transition current density for $\Psi_{1k_{\perp}}(\rho, \phi) \rightarrow \Psi_{1k_{\perp}}(\rho, \phi)$ with no transverse state transition, while the bottom panel considers the transition current density for $\Psi_{1k_{\perp}}(\rho, \phi) \rightarrow \Psi_{2k_{\perp}}(\rho, \phi)$ with an OAM change of $\Delta \ell = 1$. (c) Incoming electron plane-wave states transitioning to the pinhole state $\Psi_{k'_{\parallel}}(x, y)$. The initial state is characterized by $\mathbf{q}_{\perp} = k_x \hat{\mathbf{x}}$ in the top panel, while the middle and bottom panels involve the incident superposition plane-wave state $\Psi_{k_x k_y}^{\pi/2}(x, y)$. The bottom panel is a magnified view of the middle panel in the vicinity of the origin. (d) Transition current densities for first-order HG and LG wave functions transitioning to the Gaussian state. (e) Transition current densities for transitions from selected HG and LG states to the pinhole state. (f) Point $\hat{\mathcal{J}}_{fi}^{\perp}$ for transitions between free-electron OAM or linear momentum states which create transition current vector fields resembling the polarization vectors of light on the Poincaré sphere. The antipodal points $\{\hat{\mathcal{J}}_{0}^{\perp}, \hat{\mathcal{J}}_{1}^{\perp}\}$, $\{\hat{\mathcal{J}}_{+}^{\perp}, \hat{\mathcal{J}}_{-}^{\perp}\}$, and $\{\hat{\mathcal{J}}_{L}^{\perp}, \hat{\mathcal{J}}_{R}^{\perp}\}$ are color coded to match the box colors outlining the panels in columns (c)–(e), as well as the electron state transition arrows in Fig. 2(e).

This final state is referred to as the pinhole state as it is selected by placement of a pinhole on the TEM axis in the Fourier plane. In Fig. 3(c) it is evident that the periodicity of the plane-wave states apparent in Fig. 2(a) is inherited by the transition current density.

When prepared in a superposition plane-wave state $\psi_{k_x k_y}^{\chi}(x, y, z)$ and postselected in the diffraction plane for the pinhole state, the resulting transition current density of the probe is

$$\mathbf{J}_{k'_{\parallel}, k_x k_y}^{\chi}(x, y, z) = -\frac{e\hbar}{2\sqrt{2}mL^3}[k_x e^{ik_x x}\hat{\mathbf{x}} + k_y e^{i\chi}e^{ik_y y}\hat{\mathbf{y}}$$
$$+ Q_{\parallel}(e^{ik_x x} + e^{i\chi}e^{ik_y y})\hat{\mathbf{z}}]e^{iq_{\parallel}z}. \quad (19)$$

The phase and vector information of this transition current density are displayed in the middle and bottom panels of Fig. 3(c) for $\chi = \pi/2$ at two different magnification levels. Owing to the spatial dependence of the wave functions, the $\hat{\mathbf{x}}$ and $\hat{\mathbf{y}}$ components of Eq. (19) are functionally dependent upon x and y. It was shown in Ref. [67] when working in the dipole scattering regime, whereby $\mathbf{q}_{\perp}$ is such that $|\mathbf{q}_{\perp}|d \ll 1$, with d the transverse length scale of the target, that $\mathbf{J}_{fi}^{\perp}(\mathbf{x}_{\perp})$ becomes approximately independent of position in the vicinity

of the target. Under these circumstances when the perpendicular components of the transition current density become independent of position, $\mathbf{J}_{fi}^{\perp}(\mathbf{x}_{\perp}) \rightarrow \mathcal{J}_{fi}^{\perp}$. After normalization, $\hat{\mathcal{J}}_{fi}^{\perp} = \mathcal{J}_{fi}^{\perp}/|\mathcal{J}_{fi}^{\perp}|$ can thus be mapped onto the Poincaré sphere [Fig. 3(f)] [67]. In this limit, for $\chi = \pi/2$, the transverse component of Eq. (19) becomes circularly polarized such that it mimics the polarization of a left-handed circularly polarized photon, evident in the bottom panel of Fig. 3(c) boxed in red. All together, when $|\mathbf{q}_{\perp}|d \ll 1$, the transition current densities given by Eqs. (18) and (19) can be tailored through appropriate pre- and postselection to resemble any polarization state of light on the Poincaré sphere as shown in Fig. 3(f).

B. Bessel and Laguerre-Gauss states

By virtue of the ability to prepare free electrons in defocused-vortex (Bessel) or focused-vortex (LG) states, the corresponding transition current density can exhibit both radial and azimuthal transverse vector components. The transition current density associated with transitions between Bessel beam states $\psi_{\ell k_{\perp}}(\rho, \phi, z)$ and $\psi_{\ell' k'_{\perp}}(\rho, \phi, z)$

is [67]

$$\mathbf{J}_{\ell' k'_\perp, \ell k_\perp}(\rho, \phi, z) = \frac{i\hbar e}{2m} \Psi_{\ell k_\perp}(\rho, \phi) \Psi^*_{\ell' k'_\perp}(\rho, \phi) \left[\left(\frac{k_\perp}{2} J_{|\ell|}(k_\perp \rho)^{-1} [J_{|\ell|-1}(k_\perp \rho) - J_{|\ell|+1}(k_\perp \rho)] \right) \right.$$
$$\left. - \frac{k'_\perp}{2} J^*_{|\ell'|}(k'_\perp \rho)^{-1} [J^*_{|\ell'|-1}(k'_\perp \rho) - J^*_{|\ell'|+1}(k'_\perp \rho)] \right) \hat{\boldsymbol{\rho}} + \frac{i}{\rho}(\ell + \ell')\hat{\boldsymbol{\phi}} + iQ_\parallel \hat{\mathbf{z}} \right] e^{iq_\parallel z} \tag{20}$$

for arbitrary ℓ, $k_\perp$, ℓ', and $k'_\perp$. The transition current density for $\ell' = \ell = 1$ and $k'_\perp = k_\perp$, with $\Delta \ell = 0$, is displayed in the top panel of Fig. 3(b), showcasing the expected azimuthal character inherent to twisted electron beams. Bessel beam states can also lead to unique phase and vector profiles as seen in the bottom panel of Fig. 3(b), wherein $\Delta \ell = 1$, resulting in a transition current density with a phase structure similar to that of circularly polarized light, as well as to the wave functions shown in Fig. 2(b).

Additionally, the focused LG states in Eq. (14) can also produce transition current densities with well-defined units of OAM transferred. The transition current density for an initial LG electron state $\psi_{\ell p}(\rho, \phi, z)$ transitioning to a final state $\psi_{\ell' p'}(\rho, \phi, z)$ is given by

$$\mathbf{J}_{\ell' p', \ell p}(\rho, \phi, z) = \frac{i\hbar e}{2m} \Psi_{\ell p}(\rho, \phi) \Psi^*_{\ell' p'}(\rho, \phi) \left(\frac{1}{\rho} \left\{ (|\ell| - |\ell'|) - \frac{4\rho^2}{w_0^2} \left[L_p^{|\ell|}\left(\frac{2\rho^2}{w_0^2}\right) L_{p'}^{|\ell'|*}\left(\frac{2\rho^2}{w_0^2}\right) \right]^{-1} \left[L_{p'}^{|\ell'|*}\left(\frac{2\rho^2}{w_0^2}\right) L_p^{|\ell|+1}\left(\frac{2\rho^2}{w_0^2}\right) \right. \right. \right.$$
$$\left. \left. \left. - L_p^{|\ell|}\left(\frac{2\rho^2}{w_0^2}\right) L_{p'}^{|\ell'|+1,*}\left(\frac{2\rho^2}{w_0^2}\right) \right] \right\} \hat{\boldsymbol{\rho}} + \frac{i}{\rho}(\ell + \ell')\hat{\boldsymbol{\phi}} + iQ_\parallel \hat{\mathbf{z}} \right) e^{iq_\parallel z}, \tag{21}$$

valid for arbitrary ℓ, p, ℓ', and p'. Stemming from the commonalities in the underlying wave functions, it is unsurprising that Eqs. (20) and (21) look similar. This resemblance is most obvious when considering events wherein no transverse transition occurs, as seen when comparing the top panels of Figs. 3(a) and 3(b), for transitions between LG and Bessel states, respectively. Here, shown in the top panel of Fig. 3(a), is Eq. (21) for $p' = p = 0$ and $\ell' = \ell = 1$, which highlights the azimuthal vector component of the LG transition current density and is similar to the corresponding Bessel beam case displayed in the top panel of Fig. 3(b) for $1k_\perp$ transitioning to $1k_\perp$. The bottom panel of Fig. 3(a) shows the transition current density for $\Delta p = 1$. For inelastic-scattering events where the electron does not transfer OAM to the target, $\ell' = \ell$ and $p' = p$, and Eq. (21) reduces to

$$\mathbf{J}_{\ell' = \ell, p' = p}(\rho, \phi, z) = -\frac{\hbar e}{2mL} |\Psi_{\ell p}(\rho, \phi)|^2 \left(\frac{2\ell}{\rho}\hat{\boldsymbol{\phi}} + Q_\parallel \hat{\mathbf{z}} \right) e^{iq_\parallel z}, \tag{22}$$

which is the focused-vortex-beam form of the transition current density of a free electron moving along $\hat{\mathbf{v}} = \hat{\mathbf{z}}$ [83,85]. The azimuthal component of Eq. (22) is responsible for the spiraling behavior of the electron current typical for vortex beams and upon spatial integration over (ρ, ϕ) yields an electron current with an axial inertial OAM equal to $\ell\hbar$ [83].

C. Hermite-Gauss states

Transitions between transverse HG states that are naturally expressed in the Cartesian basis provide transition current densities with any desired $\hat{\mathbf{x}}$ or $\hat{\mathbf{y}}$ vectorial structure. Following the approach of Ref. [67], a general form for $\mathbf{J}_{n'm',nm}(x, y, z)$ involving arbitrary HG states can be derived from Eq. (4). The transition current density for $\psi_{nm}(x, y, z)$ transitioning to $\psi_{n'm'}(x, y, z)$ is

$$\mathbf{J}_{n'm',nm}(x, y, z) = \frac{i\hbar e}{2mw_0 L} \{[\sqrt{n}\Psi_{n-1,m}(x, y)\Psi^*_{n'm'}(x, y) - \sqrt{n+1}\Psi_{n+1,m}(x, y)\Psi^*_{n'm'}(x, y)$$
$$- \sqrt{n'}\Psi_{nm}(x, y)\Psi^*_{n'-1,m'}(x, y) + \sqrt{n'+1}\Psi_{nm}(x, y)\Psi^*_{n'+1,m'}(x, y)]\hat{\mathbf{x}}$$
$$+ [\sqrt{m}\Psi_{n,m-1}(x, y)\Psi^*_{n'm'}(x, y) - \sqrt{m+1}\Psi_{n,m+1}(x, y)\Psi^*_{n'm'}(x, y)$$
$$- \sqrt{m'}\Psi_{nm}(x, y)\Psi^*_{n',m'-1}(x, y) + \sqrt{m'+1}\Psi_{nm}(x, y)\Psi^*_{n',m'+1}(x, y)]\hat{\mathbf{y}}$$
$$+ iw_0 Q_\parallel \Psi_{nm}(x, y)\Psi^*_{n'm'}(x, y)\hat{\mathbf{z}}\} e^{iq_\parallel z} \tag{23}$$

for arbitrary n, m, n', and m'. As seen in the form of the perpendicular component of Eq. (23), careful choice regarding the pre- and postselection of the initial and final HG transverse electron states can be intuited to yield a transition current density with nontrivial $\hat{\mathbf{x}}$ or $\hat{\mathbf{y}}$ vectorial behavior in the plane orthogonal to the direction of propagation. Working in the $\ell = \pm 1$ OAM Hilbert space, $\mathbf{J}_{n'm',nm}(x, y, z)$ is displayed in the column of Fig. 3(d) for first-order

electron wave functions $\psi_{10}(x, y, z)$ and $\psi_{01}(x, y, z)$, and their linear combination $\psi_{10,01}^{\chi=\pi/2}(x, y, z) = (1/\sqrt{2L})[\psi_{10}(x, y, z) + \psi_{01}(x, y, z)e^{i\pi/2}]$, respectively, all transitioning to the final Gaussian wave function $\psi_{00}(x, y, z) = (1/\sqrt{L})\Psi_{00}(x, y)e^{ik_\parallel z}$. In the zero-width limit whereby $w_0 \to 0$, for the first-order transitions discussed above, the transverse components of the transition current density become spatially independent and $\mathbf{J}_{fi}^\perp(\mathbf{x}) \to \mathcal{J}_{fi}^\perp$. Under these constraints, the transition current

density unit vector $\mathcal{J}_{fi}^{\perp}$ can thus imitate the polarization vector $\hat{\boldsymbol{\epsilon}}$ of free-space light, as illustrated on the electron analog of the Poincaré sphere presented in Fig. 3(f). When no transverse transition of the probe occurs, i.e., $n' = n$ and $m' = m$ in Eq. (23), the transition current density reduces to

$$\mathbf{J}_{n'=n,m'=m}(x,y,z) = -\frac{e\hbar}{2mL}Q_{\parallel}|\Psi_{nm}(x,y)|^2 e^{iq_{\parallel}z}\hat{\mathbf{z}}, \quad (24)$$

which is oriented parallel to the TEM axis regardless of the values for n and m. In the zero-width limit, Eq. (24) reduces to the classical current of a point electron source [51] when $n = m = 0$. Overall, the purely longitudinal behavior of Eq. (24) differs from the vortex-electron-beam case in Eq. (22) wherein the current density has a $\hat{\boldsymbol{\phi}}$ component perpendicular to the electron's direction of motion.

Alternatively, when the nm HG state transitions to the forward-directed pinhole state rather than a transversely focused Gaussian state, the transition current density becomes

$$\mathbf{J}_{k_{\parallel}',nm}(x,y,z)$$
$$= \frac{i\hbar e}{2mw_0L^2}\{[\sqrt{n}\Psi_{n-1,m}(x,y) - \sqrt{n+1}\Psi_{n+1,m}(x,y)]\hat{\mathbf{x}}$$
$$+ [\sqrt{m}\Psi_{n,m-1}(x,y) - \sqrt{m+1}\Psi_{n,m+1}(x,y)]\hat{\mathbf{y}}$$
$$+ iw_0Q_{\parallel}\Psi_{n,m}(x,y)\hat{\mathbf{z}}\}e^{iq_{\parallel}z}. \quad (25)$$

Equation (25) is displayed in Fig. 3(e) for the same initial HG states as those used in Fig. 3(d), transitioning instead to the pinhole state $\psi_{k_{\parallel}'}(x,y,z)$. For the focused superposition state $\psi_{10,01}^{\chi}(x,y,z) = (1/\sqrt{2L})[\psi_{10}(x,y,z) + \psi_{01}(x,y,z)e^{i\chi}]$ transitioning to the pinhole state $\psi_{k_{\parallel}'}(x,y,z)$, the transition current density explicitly has the form

$$\mathbf{J}_{k_{\parallel}',10,01}^{\chi}(x,y,z)$$
$$= \frac{i\hbar e}{2\sqrt{2}mw_0L^2}([\Psi_{00}(x,y) - \sqrt{2}\Psi_{20}(x,y)$$
$$- \Psi_{11}(x,y)e^{i\chi}]\hat{\mathbf{x}}$$
$$+ \{[\Psi_{00}(x,y) - \sqrt{2}\Psi_{02}(x,y)]e^{i\chi} - \Psi_{11}(x,y)\}\hat{\mathbf{y}}$$
$$+ iw_0Q_{\parallel}[\Psi_{10}(x,y) + \Psi_{01}(x,y)e^{i\chi}]\hat{\mathbf{z}})e^{iq_{\parallel}z}. \quad (26)$$

The difference between Eqs. (19) and (26) originates from the choice of the initial electron wave function being either a superposition of linear momentum or OAM states, respectively. Imposing the same conditions placed upon the wave functions in Eq. (23) to obtain a transition current density whose transverse vectorial components are spatially independent, Eqs. (25) and (26) can be used to construct transition current

densities on the surface of the Poincaré sphere as presented in Fig. 3(f). Therefore, transitions between specific states on the Bloch sphere [Fig. 2(e)] produce transition current densities which mimic the polarization structure of free-space light and can thus be mapped onto the Poincaré sphere [Fig. 3(f)].

V. STATE- AND ENERGY-RESOLVED OBSERVABLES

Building from Secs. II–IV, in this section the EEL, EEG, and DDCS observables between phase-shaped states of the electron probe are derived. Measurements of EEL and EEG processes are discussed first, including the narrow-beam-width limit common in the low-loss electron-scattering regime, before moving on to presentation of the DDCS. A comparison of the EEL and EEG scattering processes, and their relation to the properties of the transition current density under interchange of initial and final electron states are briefly presented. We illustrate that the transversely phase-shaped EEL, EEG, and DDCS observables reduce to the familiar forms found in the literature under the appropriate limits.

A. Electron-energy-loss and -gain probabilities in the narrow-beamwidth limit

In considering low-loss EEL and EEG scattering events in the narrow-beamwidth limit appropriate to the STEM it is customary to work within the nonrecoil approximation, where the change in the energy of the electron is dictated entirely by its momentum change along the axis of propagation [51]. In this limit, the forward recoil momentum $\hbar q_{\parallel}\hat{\mathbf{z}}$ is small compared to the electron's initial momentum $\hbar\mathbf{k}_i$, so its change in energy can be approximated by $\hbar\varepsilon_{if} = \sqrt{(mc^2)^2 + (\hbar c\mathbf{k}_i)^2} - \sqrt{(mc^2)^2 + [\hbar c(\mathbf{k}_i - \mathbf{q})]^2} \approx \hbar\mathbf{v}_i \cdot \mathbf{q}$, where $\hbar\mathbf{k}_i/m = \gamma_i\mathbf{v}_i$ and $\hbar\mathbf{k}_i = \mathbf{p}_i$ for relativistic matter waves. Upon insertion of $\varepsilon_{if} = \mathbf{v}_i \cdot \mathbf{q}$ into the trailing δ function in Eq. (9), the state- and frequency-resolved EEL rate becomes

$$w_{fi}^{\text{loss}}(\omega) = -\frac{8\pi}{\hbar v_i}\int d\mathbf{x}\,d\mathbf{x}'\text{Im}[\mathbf{J}_{fi}^*(\mathbf{x}) \cdot \overset{\leftrightarrow}{\mathbf{G}}(\mathbf{x},\mathbf{x}',\omega) \cdot \mathbf{J}_{fi}(\mathbf{x}')]$$
$$\times \delta(q_{\parallel} - \omega/v_i), \quad (27)$$

where $\overset{\leftrightarrow}{\mathbf{G}}(\mathbf{x},\mathbf{x}',\omega)$ is the target's electromagnetic Green's tensor introduced in Sec. II. The state- and energy-resolved EEL probability $P_{fi}^{\text{loss}}(\omega) = (L/v_i)w_{fi}^{\text{loss}}(\omega)$ is obtained by integrating Eq. (27) over the time it takes the probe electron to traverse the path length L as it interacts with the target specimen. From $P_{fi}^{\text{loss}}(\omega)$, the state- and energy-resolved EEL probability is determined by summing over all possible final electron states with $\sum_{k_{\parallel}^f} \to +(L/2\pi)\int_{-\infty}^{\infty}dq_{\parallel}$ and dividing by $\hbar$, resulting in the EEL probability per unit energy

$$\Gamma_{fi}^{\text{loss}}(\omega) = -\frac{4}{\hbar^2}\int d\mathbf{x}\,d\mathbf{x}'\text{Im}\left[\left(\frac{L}{v_i}\right)\mathbf{J}_{fi}^*\left(\mathbf{x};q_{\parallel} = \frac{\omega}{v_i}\right) \cdot \overset{\leftrightarrow}{\mathbf{G}}(\mathbf{x},\mathbf{x}',\omega) \cdot \left(\frac{L}{v_i}\right)\mathbf{J}_{fi}\left(\mathbf{x}';q_{\parallel} = \frac{\omega}{v_i}\right)\right]. \quad (28)$$

Here $\mathbf{J}_{fi}(\mathbf{x};q_{\parallel}=\omega/v_i)=\mathbf{J}_{fi}(\mathbf{x})|_{q_{\parallel}=\omega/v_i}=\mathbf{J}_{fi}(\mathbf{x}_{\perp})e^{iq_{\parallel}z}|_{q_{\parallel}=\omega/v_i} = \mathbf{J}_{fi}(\mathbf{x}_{\perp})e^{i(\omega/v_i)z}$ makes explicit the locking of the longitudinal recoil wave number $q_{\parallel}$ to ω/v_i imposed by the nonrecoil approximation in Eqs. (27) and (28). Due to the frequent

appearance of the L/v_i factor here and in the following equations, we define a new transition current as $\mathbf{J}_{fi}(\mathbf{x}, \omega = q_{\parallel}v_i) \equiv (L/v_i)\mathbf{J}_{fi}(\mathbf{x};q_{\parallel} = \omega/v_i)$ with dimensions of charge flux per unit frequency. For clarity, we also abandon the general

notation $\mathbf{x} = (\mathbf{x}_\perp, z)$ in favor of $\mathbf{x} = (\mathbf{R}, z)$, as is common in the low-loss STEM EEL and EEG literature.

Using the current $\mathbf{J}_{fi}(\mathbf{x}, \omega = q_\| v_i)$, the EEL probability can also be cast in terms of the target's transition electric field $\mathbf{E}_{fi}(\mathbf{x}, \omega = q_\| v_i) = -4\pi i\omega \int d\mathbf{x}' \overleftrightarrow{\mathbf{G}}(\mathbf{x}, \mathbf{x}', \omega) \cdot$

$\mathbf{J}_{fi}(\mathbf{x}', \omega = q_\| v_i)$ resolved in frequency. Here $\mathbf{E}_{fi}$ represents the electric field produced by the target in response to stimulation by the probing electron. Expressed in terms of this field, the EEL probability per unit energy becomes

$$\Gamma_{fi}^{\mathrm{loss}}(\omega) = -\frac{1}{\pi \hbar^2 \omega} \mathrm{Re}\left(\int d\mathbf{x}\, \mathbf{J}_{fi}^*(\mathbf{x}, \omega = q_\| v_i) \cdot \mathbf{E}_{fi}(\mathbf{x}, \omega = q_\| v_i) \right), \tag{29}$$

which recovers the classical relationship [51,86] between $\Gamma_{fi}^{\mathrm{loss}}(\omega)$ and the work performed by the electron against its own induced field. When the electron beam waist w_0 is negligible compared to the length scale over which the response field changes, $\mathbf{E}_{fi}$ can be taken as constant over the spatial domain where the current density is appreciable and approximated by its value $\mathbf{E}_{fi}(\mathbf{R}, z, \omega = q_\| v_i) \approx \mathbf{E}_{fi}(\mathbf{R}_0, z, \omega = q_\| v_i)$ at the impact parameter $\mathbf{R}_0$. In this narrow-beamwidth limit, Eq. (29) becomes

$$\Gamma_{fi}^{\mathrm{loss}}(\mathbf{R}_0, \omega) = -\frac{1}{\pi \hbar^2 \omega} \mathrm{Re}\left[\int dz \left(\int d\mathbf{R}\, \mathbf{J}_{fi}^*(\mathbf{R}, z, \omega = q_\| v_i) e^{i\omega z/v_i} \right) e^{-i\omega z/v_i} \cdot \mathbf{E}_{fi}(\mathbf{R}_0, z, \omega = q_\| v_i) \right]$$

$$= -\frac{1}{\pi \hbar^2 \omega} \mathrm{Re}\left(\mathcal{J}_{fi}^* \cdot \int dz\, \mathbf{E}_{fi}(\mathbf{R}_0, z, \omega = q_\| v_i) e^{-i\omega z/v_i} \right), \tag{30}$$

where the transition current $\mathcal{J}_{fi} = \int d\mathbf{R}\, \mathbf{J}_{fi}(\mathbf{R}, z, \omega = q_\| v_i) e^{-i\omega z/v_i} = (-e/mv_i)[\langle \Psi_f | \hat{\mathbf{p}}_\perp | \Psi_i \rangle + (\hbar Q_\|/2)\langle \Psi_f | \Psi_i \rangle \hat{\mathbf{z}}]$ is z and ω independent. It has the transverse and longitudinal components $\mathcal{J}_{fi}^\perp = -(e/mv_i)\langle \Psi_f | \hat{\mathbf{p}}_\perp | \Psi_i \rangle$ and $\mathcal{J}_{fi}^\| = -(\hbar e Q_\|/2mv_i)\langle \Psi_f | \Psi_i \rangle \hat{\mathbf{z}}$, respectively, which allow the EEL probability in Eq. (30) to be separated into the perpendicular and parallel contributions

$$\Gamma_{fi\perp}^{\mathrm{loss}}(\mathbf{R}_0, \omega) = -\frac{1}{\pi \hbar^2 \omega} \mathrm{Re}\left(\mathcal{J}_{fi}^{\perp *} \cdot \int dz\, \mathbf{E}_{fi}(\mathbf{R}_0, z, \omega = q_\| v_i) e^{-i\omega z/v_i} \right),$$

$$\Gamma_{fi\|}^{\mathrm{loss}}(\mathbf{R}_0, \omega) = -\frac{1}{\pi \hbar^2 \omega} \mathrm{Re}\left(\mathcal{J}_{fi}^{\| *} \cdot \int dz\, \mathbf{E}_{fi}(\mathbf{R}_0, z, \omega = q_\| v_i) e^{-i\omega z/v_i} \right). \tag{31}$$

Based on the forms of $\mathcal{J}_{fi}^\perp$ and $\mathcal{J}_{fi}^\|$ above, it is evident that $\mathcal{J}_{fi}^\perp = \mathbf{0}$ and $\mathcal{J}_{fi}^\| = -(\hbar e Q_\|/2mv_i)\hat{\mathbf{z}}$ in the event of no transverse transition, i.e., $\Psi_i = \Psi_f$ and $\Gamma_{fi\perp}^{\mathrm{loss}} = 0$, while $\mathcal{J}_{fi}^\perp \neq \mathbf{0}$ and $\mathcal{J}_{fi}^\| = \mathbf{0}$ when a transition occurs in the probe's transverse wave function, i.e., $\Psi_i \neq \Psi_f$ and $\Gamma_{fi\|}^{\mathrm{loss}} = 0$. In the former case, $\Gamma_{fi\|}^{\mathrm{loss}}(\mathbf{R}_0, \omega)$ in Eq. (31) reduces to the the well-known classical form for the EEL probability [51,69,87,88] in the zero-width limit $w_0 \to 0$. Specifically, $\Gamma_{fi\|}^{\mathrm{loss}}(\mathbf{R}_0, \omega) \to \Gamma_{\mathrm{cl}}(\mathbf{R}_0, \omega) = -(2e/\hbar)^2 \int dz\, dz' \mathrm{Im}[\hat{\mathbf{z}} \cdot \overleftrightarrow{\mathbf{G}}(\mathbf{R}_0, z; \mathbf{R}_0, z', \omega) \cdot \hat{\mathbf{z}} e^{-i\omega(z-z')/v_i}]$, which is the EEL probability per unit energy for a uniformly moving classical electron with current density $\mathbf{J}_{\mathrm{cl}}(\mathbf{x}, \omega) = -e\delta(\mathbf{R} - \mathbf{R}_0)e^{i\omega z/v_i}\hat{\mathbf{z}}$ at impact parameter $\mathbf{R}_0$.

To construct the laser-stimulated phase-shaped EEG observable in the narrow-beamwidth limit, we again introduce $\varepsilon_{if} = \mathbf{v}_i \cdot \mathbf{q}$ into the trailing δ function in the frequency-resolved EEG rate presented in Eq. (11). As a result, the state- and frequency-resolved EEG rate and scattering probability are

$$w_{fi}^{\mathrm{gain}}(\omega) = \frac{2\pi}{v_i}\left(\frac{1}{\hbar\omega_\nu} \right)^2 \left| \int d\mathbf{x}\, \mathbf{E}_\nu^{(+)}(\mathbf{x}) \cdot \mathbf{J}_{fi}(\mathbf{x}) \right|^2 \delta(q_\| + \omega/v_i)\delta(\omega - \omega_{\nu\nu'}) \tag{32}$$

and $P_{fi}^{\mathrm{gain}}(\omega) = (L/v_i) w_{fi}^{\mathrm{gain}}(\omega)$, respectively. In parallel to loss, the EEG probability per unit energy is determined from $P_{fi}^{\mathrm{gain}}(\omega)$ after integrating over final states $\sum_{k_\|^f} \to +(L/2\pi) \int_{-\infty}^{\infty} dq_\|$ and dividing by $\hbar$, resulting in

$$\Gamma_{fi}^{\mathrm{gain}}(\omega) = \frac{1}{\hbar}\left(\frac{1}{\hbar\omega_\nu} \right)^2 \left| \int d\mathbf{x}\, \mathbf{E}_\nu^{(+)}(\mathbf{x}) \cdot \mathbf{J}_{fi}(\mathbf{x}, \omega = -q_\| v_i) \right|^2 \delta(\omega - \omega_{\nu\nu'}). \tag{33}$$

As in the case of loss, if the target's induced electric field varies little over the spatial domain of the probe's transition current density, then $\mathbf{E}_\nu^{(+)}(\mathbf{R}, z) \approx \mathbf{E}_\nu^{(+)}(\mathbf{R}_0, z)$ to lowest order and the state- and energy-resolved EEG probability takes the form

$$\Gamma_{fi}^{\mathrm{gain}}(\mathbf{R}_0, \omega) = \frac{1}{\hbar}\left(\frac{1}{\hbar\omega_\nu} \right)^2 \left| \int dz\, \mathbf{E}_\nu^{(+)}(\mathbf{R}_0, z) e^{-i\omega z/v_i} \cdot \left(\int d\mathbf{R}\, \mathbf{J}_{fi}(\mathbf{R}, z, \omega = -q_\| v_i) e^{i\omega z/v_i} \right) \right|^2 \delta(\omega - \omega_{\nu\nu'})$$

$$= \frac{1}{\hbar}\left(\frac{1}{\hbar\omega_\nu} \right)^2 \left| \int dz\, e^{-i\omega z/v_i} \mathbf{E}_\nu^{(+)}(\mathbf{R}_0, z) \cdot \mathcal{J}_{fi} \right|^2 \delta(\omega - \omega_{\nu\nu'}), \tag{34}$$

with z- and ω-independent transition current $\mathcal{J}_{fi}$ defined below Eq. (30). As in the case of EEL, the EEG probability can also be broken into perpendicular and parallel components

$$\Gamma_{fi\perp}^{\text{gain}}(\mathbf{R}_0, \omega) = \frac{1}{\hbar}\left(\frac{1}{\hbar\omega_\nu}\right)^2 |\mathcal{J}_{fi}^\perp|^2 \left|\int dz\, e^{-i\omega z/v_i} \mathbf{E}_\nu^{(+)}(\mathbf{R}_0, z) \cdot \hat{\boldsymbol{\mathcal{J}}}_{fi}^\perp\right|^2 \delta(\omega - \omega_{\nu\nu'}),$$

$$\Gamma_{fi\|}^{\text{gain}}(\mathbf{R}_0, \omega) = \frac{1}{\hbar}\left(\frac{1}{\hbar\omega_\nu}\right)^2 |\mathcal{J}_{fi}^\||^2 \left|\int dz\, e^{-i\omega z/v_i} \mathbf{E}_\nu^{(+)}(\mathbf{R}_0, z) \cdot \hat{\boldsymbol{\mathcal{J}}}_{fi}^\|\right|^2 \delta(\omega - \omega_{\nu\nu'}), \tag{35}$$

where $\boldsymbol{\mathcal{J}}_{fi} = \hat{\boldsymbol{\mathcal{J}}}_{fi}|\mathcal{J}_{fi}| = \hat{\boldsymbol{\mathcal{J}}}_{fi}\mathcal{J}_{fi}$. Similarly, when the transverse wave functions $\Psi_i = \Psi_f$, $\Gamma_{fi}^{\text{gain}}(\mathbf{R}_0, \omega) = \Gamma_{fi\|}^{\text{gain}}(\mathbf{R}_0, \omega)$ and one recovers the conventional EEG probability [51,66,70–72] in the narrow-beam limit $w_0 \to 0$. Through combination of optical polarization and pre- and postselection of the probe's transverse phase profile to define its polarization, cross-polarized measurements in the STEM can be leveraged to directly interrogate optically excited target mode symmetries in three dimensions with nanoscale spatial resolution [66].

The above expressions for EEL and EEG probabilities involve interrogation of the target's induced response field by the transition current densities $\mathbf{J}_{fi}(\mathbf{x}, \omega = +q_\| v_i)$ and $\mathbf{J}_{fi}(\mathbf{x}, \omega = -q_\| v_i)$ of the probe. It is natural to consider the relationship between these currents upon interchanging initial and final probe states in both the transverse and axial directions. The reciprocal behavior of pre- and postselection of the probe's transverse states, i.e., $\mathbf{J}_{fi}^\perp(\mathbf{R}) = \mathbf{J}_{if}^{\perp*}(\mathbf{R})$, were discussed previously in Sec. IV. Additionally, along the TEM axis, the longitudinal component $J_{fi}^\|(\mathbf{R}) = J_{if}^{\|*}(\mathbf{R})$ expresses the relationship between anti-Stokes (EEG) and Stokes (EEL) scattering processes at the level of the transition current density. Taken together,

$$\mathbf{J}_{fi}(\mathbf{x}, \omega = +q_\| v_i) = \left(\frac{L}{v_i}\right)[\mathbf{J}_{if}^{\perp*}(\mathbf{R}) + J_{if}^{\|*}(\mathbf{R})\hat{\mathbf{z}}]e^{i(\omega/v_i)z} = \left(\frac{L}{v_i}\right)\{[\mathbf{J}_{if}^\perp(\mathbf{R}) + J_{if}^\|(\mathbf{R})\hat{\mathbf{z}}]e^{-i(\omega/v_i)z}\}^* = \mathbf{J}_{if}^*(\mathbf{x}, \omega = -q_\| v_i). \tag{36}$$

These symmetries of the transition current density under interchange of initial and final states, and their effect on the observables, are detailed further in the Appendix.

B. Double-differential inelastic-scattering cross section in the wide-field limit

When dealing with plane-wave electron states, the scattering cross section is a common observable of interest. It is attained from the EEL transition rate $w_{fi}^{\text{loss}}(\omega)$ in Eq. (9) by first summing over the electron final states $\sum_{\mathbf{k}_f} \to (L/2\pi)^3 \int d\mathbf{k}_f$ and subsequently dividing by the incoming plane-wave particle flux $\hbar k_i/mL^3$. The total frequency-resolved scattering cross section is given by

$$\sigma(\omega) = \frac{mL^3}{\hbar k_i}\left(\frac{L}{2\pi}\right)^3 \int d\Omega_f k_f^2 dk_f\, w_{fi}(\omega), \tag{37}$$

and by integration over frequency, the angle-resolved scattering cross section is

$$\frac{\partial\sigma}{\partial\Omega_f} = \frac{mL^3}{\hbar k_i}\left(\frac{L}{2\pi}\right)^3 \int d\omega\, k_f^2 dk_f\, w_{fi}(\omega) = -\frac{mL^3}{\hbar k_i}\left(\frac{L}{2\pi}\right)^3 \int d\omega\, dE_{if}\left(\frac{\gamma_f m}{\hbar^2 k_f}\right) k_f^2 w_{fi}(\omega), \tag{38}$$

where $dE_{if} = -(\hbar^2/m)k_f dk_f$ and $d\Omega_f = \sin\theta_f d\theta_f d\phi_f$. Finally, noting that $\partial\sigma/\partial\Omega_f = \int dE_{if}\partial^2\sigma/(\partial E_{if}\partial\Omega_f)$, the DDCS is defined as

$$\frac{\partial^2\sigma}{\partial E_{if}\partial\Omega_f} = -\frac{m^2 L^3}{\hbar^3}\left(\frac{L}{2\pi}\right)^3\left(\frac{k_f}{k_i}\right)\int d\omega\, w_{fi}(\omega)$$

$$= \left(\frac{mL^3}{\pi\hbar^2}\right)^2\left(\frac{k_f}{k_i}\right)\int d\omega\, d\mathbf{x}\, d\mathbf{x}'\text{Im}[\mathbf{J}_{fi}^*(\mathbf{x}) \cdot \overset{\leftrightarrow}{\mathbf{G}}(\mathbf{x}, \mathbf{x}', \omega) \cdot \mathbf{J}_{fi}(\mathbf{x}')]\delta(\omega - \varepsilon_{if}), \tag{39}$$

which reduces to the DDCS common for an isolated dipolar target (41) in core-loss EEL scattering [37,67,89] when the electrostatic limit where $c \to \infty$ is taken. Further analytic progress is possible in the case of a single target dipole located at position $\mathbf{x}_d$ and characterized by frequency-dependent polarizability tensor $\overset{\leftrightarrow}{\boldsymbol{\alpha}}(\omega)$. In this case, the induced Green's function reduces to $\overset{\leftrightarrow}{\mathbf{G}}(\mathbf{x}, \mathbf{x}', \omega) = -(4\pi\omega^2)\overset{\leftrightarrow}{\mathbf{G}}^0(\mathbf{x}, \mathbf{x}_d, \omega) \cdot \overset{\leftrightarrow}{\boldsymbol{\alpha}}(\omega) \cdot \overset{\leftrightarrow}{\mathbf{G}}^0(\mathbf{x}_d, \mathbf{x}', \omega)$, where $\overset{\leftrightarrow}{\mathbf{G}}^0(\mathbf{x}, \mathbf{x}', \omega) = -(1/4\pi\omega^2)[(\omega/c)^2\overset{\leftrightarrow}{\mathbf{I}} + \nabla\nabla]e^{i(\omega/c)|\mathbf{x}-\mathbf{x}'|}/|\mathbf{x} - \mathbf{x}'|$ is the vacuum dipole Green's function, and the DDCS can be expressed analytically. Specifically, with a single incoming plane wave scattering to a single outgoing plane wave as described by the transition current density given by Eq. (18), the fully retarded DDCS becomes

$$\frac{\partial^2\sigma}{\partial E_{if}\partial\Omega_f} = \frac{e^2}{\hbar^2\pi}\left(\frac{k_f}{k_i}\right)\frac{1}{\varepsilon_{if}^2}\text{Im}\left\{\mathbf{Q} \cdot \left[\left(\frac{\varepsilon_{if}}{c}\right)^2\overset{\leftrightarrow}{\mathbf{I}} - \mathbf{qq}\right] \cdot \frac{\overset{\leftrightarrow}{\boldsymbol{\alpha}}(\varepsilon_{if})}{|(\varepsilon_{if}/c)^2 - q^2|^2} \cdot \left[\left(\frac{\varepsilon_{if}}{c}\right)^2\overset{\leftrightarrow}{\mathbf{I}} - \mathbf{qq}\right] \cdot \mathbf{Q}\right\}, \tag{40}$$

where $\mathbf{Q} = 2\mathbf{k}_i - \mathbf{q}$. In the quasistatic limit ($c \to \infty$), Eq. (40) reduces to the more familiar form [90]

$$\frac{\partial^2 \sigma}{\partial E_{if} \partial \Omega} = \frac{e^2}{\hbar^2 \pi} \left(\frac{k_f}{k_i} \right) \frac{1}{\varepsilon_{if}^2} \mathrm{Im} \left(\mathbf{Q} \cdot \mathbf{qq} \cdot \frac{\overset{\leftrightarrow}{\boldsymbol{\alpha}}(\varepsilon_{if})}{q^4} \cdot \mathbf{qq} \cdot \mathbf{Q} \right). \tag{41}$$

VI. NUMERICAL IMPLEMENTATION

This section details the numerical implementation of the inelastic-scattering observables presented above in Secs. V A and V B for transversely phase-structured free electrons in both the focused-beam and wide-field limits. Our implementation generalizes the electron-driven discrete dipole approximation (*e*-DDA) [91,92], built on top of the DDSCAT [93] framework, which previously utilized the vacuum electric field $\mathbf{E}_{fi}^0$ of a point electron as the source instead of an optical plane-wave field. Other fully retarded and quasistatic numerical methods for simulating extended nanophotonic targets have been formulated to model low-loss electron-beam interactions, such as the finite-difference time-domain [94,95], metal nanoparticle boundary-element (MNPBEM) [96], and finite-element [97,98] methods. In addition, transversely structured electron beams have been implemented in the MNPBEM [60,63,65,68], albeit in the quasistatic limit only. Our treatment of the inelastic scattering of transversely structured electron beams in the *e*-DDA is distinguished by its incorporation of fully retarded electron-sample interactions in both focused-beam and wide-field limits.

The *e*-DDA and DDA originate from the method of coupled dipoles [99], whereby the target is discretized into a finite collection of point electric dipoles

$$\mathbf{p}_k(\omega) = \sum_{l=1}^{N} [\overset{\leftrightarrow}{\boldsymbol{\alpha}}(\omega)^{-1} - (-4\pi \omega^2)\overset{\leftrightarrow}{\mathbf{G}}^0(\omega)]_{kl}^{-1} \cdot \mathbf{E}_{fi}^0(\mathbf{x}_l, \omega) \tag{42}$$

of polarizability $\overset{\leftrightarrow}{\boldsymbol{\alpha}}(\omega)$, each driven by the vacuum transition field $\mathbf{E}_{fi}^0(\mathbf{x}_i, \omega)$ at frequency ω and mutually interacting via their fully retarded electric dipole fields $-4\pi \omega^2 \sum_l \overset{\leftrightarrow}{\mathbf{G}}_{kl}^0(\omega) \cdot \mathbf{p}_l(\omega)$ until reaching self-consistency at that same frequency. Here $\overset{\leftrightarrow}{\mathbf{G}}_{kl}^0(\omega)$ are the kl-matrix elements of the vacuum dipole Green's function $\overset{\leftrightarrow}{\mathbf{G}}^0(\mathbf{x}, \mathbf{x}', \omega)$.

Upon inversion of Eq. (42), all EEL observables described above may be calculated from the resulting $\mathbf{p}_k(\omega)$ together with the applied field $\mathbf{E}_{fi}^0(\mathbf{x}_k, \omega)$ [Eq. (A1)] evaluated at each dipole. Specifically, the focused-beam EEL probability and the wide-field DDCS expressions in Eqs. (28) and (39), respectively, can be adapted to a form that is compatible with the *e*-DDA code via the EEL rate per unit frequency

$$w_{fi}^{\mathrm{loss}}(\omega) = -\frac{8\pi}{\hbar} \int d\mathbf{x} \, d\mathbf{x}' \mathrm{Im}[\mathbf{J}_{fi}^*(\mathbf{x}) \cdot \overset{\leftrightarrow}{\mathbf{G}}(\mathbf{x}, \mathbf{x}', \omega) \cdot \mathbf{J}_{fi}(\mathbf{x}')]$$
$$\times \, \delta(\omega - \varepsilon_{if})$$
$$= \frac{2}{\hbar} \left(\frac{v_i}{L} \right)^2 \mathrm{Im} \left(\sum_k \mathbf{E}_{fi}^{0*}(\mathbf{x}_k, \omega) \cdot \mathbf{p}_k(\omega) \right) \delta(\omega - \varepsilon_{if}). \tag{43}$$

Here the target's induced Green's function $\overset{\leftrightarrow}{\mathbf{G}}(\mathbf{x}, \mathbf{x}', \omega)$ is expanded in terms of the polarizabilities of the N dipoles representing the target. Specifically,

$$\overset{\leftrightarrow}{\mathbf{G}}(\mathbf{x}, \mathbf{x}', \omega) = -4\pi \omega^2 \sum_{jj'} \overset{\leftrightarrow}{\mathbf{G}}^0(\mathbf{x}, \mathbf{x}_j, \omega) \cdot [\overset{\leftrightarrow}{\boldsymbol{\alpha}}^{-1}(\omega)$$
$$- (-4\pi \omega^2)\overset{\leftrightarrow}{\mathbf{G}}^0(\omega)]_{jj'}^{-1} \cdot \overset{\leftrightarrow}{\mathbf{G}}^0(\mathbf{x}_{j'}, \mathbf{x}', \omega), \tag{44}$$

which can be derived from the response field of a polarizable body described in terms of its induced Green's function $\overset{\leftrightarrow}{\mathbf{G}}(\mathbf{x}, \mathbf{x}', \omega)$ driven by the external current density $\mathbf{J}^0(\mathbf{x})$ or by the free propagation [via $\overset{\leftrightarrow}{\mathbf{G}}^0(\mathbf{x}, \mathbf{x}', \omega)$] of the target's induced current density $\mathbf{J}(\mathbf{x}) = \sum_j (-i\omega)\mathbf{p}_j(\omega)\delta(\mathbf{x} - \mathbf{x}_j)$ as $\mathbf{E}(\mathbf{x}, \omega) = -4\pi i\omega \int d\mathbf{x}' \overset{\leftrightarrow}{\mathbf{G}}(\mathbf{x}, \mathbf{x}', \omega) \cdot \mathbf{J}^0(\mathbf{x}') = -4\pi i\omega \int d\mathbf{x}' \overset{\leftrightarrow}{\mathbf{G}}^0(\mathbf{x}, \mathbf{x}', \omega) \cdot \mathbf{J}(\mathbf{x}')$.

A. Numerical evaluation of state- and energy-resolved EEL and EEG probabilities

From Eq. (43), the state- and energy-resolved EEL probability can be obtained following the same procedure as in Sec. V A. Specifically, the transversely phase-shaped EEL probability becomes

$$\Gamma_{fi}^{\mathrm{loss}}(\omega) = \frac{1}{\pi \hbar^2} \mathrm{Im} \left(\sum_k \mathbf{E}_{fi}^{0*}(\mathbf{x}_k, \omega = q_\parallel v_i) \cdot \mathbf{p}_k(\omega = q_\parallel v_i) \right), \tag{45}$$

when working within the nonrecoil approximation introduced in Sec. V, as appropriate to focused beams prepared in the STEM configuration. The vacuum transition electric field $\mathbf{E}_{fi}^0$ appearing within Eqs. (42) and (45) can, in principle, be any of the fields sourced by the transversely focused transition current densities described in Sec. IV. However, due to their complexity, only those transitions involving OAM transfers $\Delta \ell = 1$ depicted as colored arrows in Fig. 2(e) and more specifically the resulting electric fields sourced by the transition current densities seen in Figs. 3(c) and 3(d) have been implemented within the *e*-DDA code. Explicit forms for these fields are provided in the Appendix. Phase-shaped EEG probability spectra of nanophotonic targets under continuous-wave laser stimulation can also be evaluated numerically using the *e*-DDA as detailed previously [66]. Briefly, the EEG probability in Eq. (34) is numerically integrated by quadrature using the optically induced response field of the target $\mathbf{E}_\nu^{(+)}$ calculated using DDSCAT and the $\hat{\mathbf{J}}_{fi}$ defined by selection of a specific pair of incoming and outgoing free-electron states.

Figure 4 presents a comparison of normalized focused-beam EEL and EEG spectra for a 25-nm-radius silver sphere calculated using *e*-DDA with dielectric data taken from Ref. [100]. Probing electrons have a speed of $0.7c$. Figure 4(a) shows phase-structured EEL (solid traces) and EEG (dashed traces) spectra at impact parameter $\mathbf{R}_0 = (1/\sqrt{2})(40 \text{ nm}, 40 \text{ nm})$. The optical excitation polarization $\hat{\boldsymbol{\epsilon}}$ in the EEG calculations is along $\hat{\mathbf{x}}$. Gray and magenta colors correspond to pre- and postselection of HG transitions $\Psi_{00}(x, y) \to \Psi_{00}(x, y)$ with $\hat{\mathcal{J}}_{fi}^\parallel = \hat{\mathbf{z}}$ and $\Psi_{10}(x, y) \to \Psi_{00}(x, y)$ with $\hat{\mathcal{J}}_{fi}^\perp = \hat{\mathbf{x}}$, respectively. While the *e*-DDA calculations can capture coupling to the higher-order multipoles,
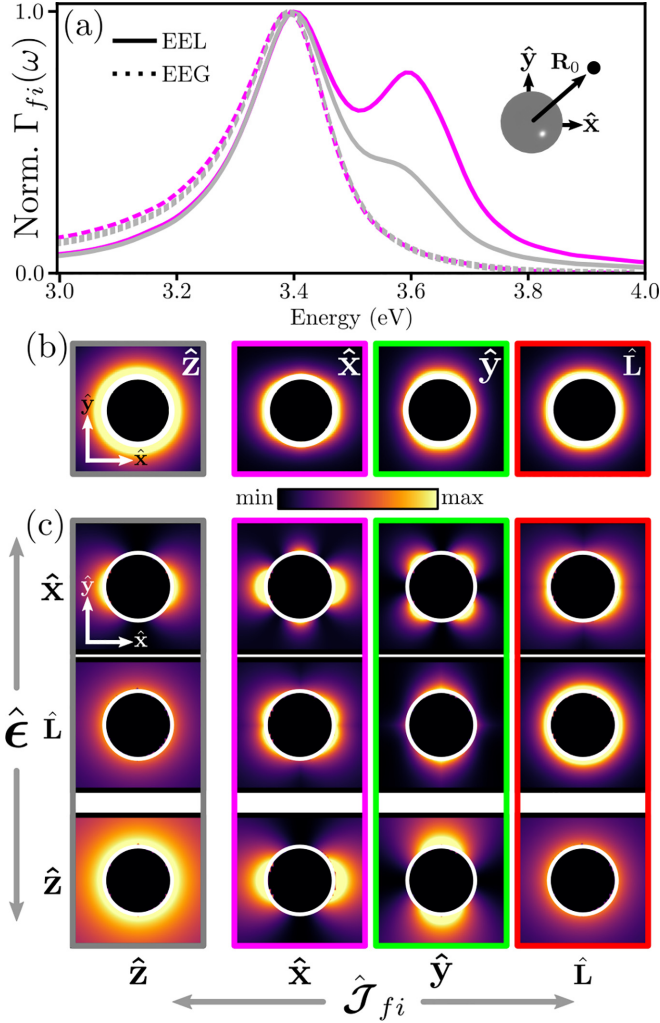
FIG. 4. Phase-shaped EEL and EEG point spectra and spectrum images of a silver plasmonic sphere of 25 nm radius evaluated using the *e*-DDA. (a) Phase-shaped EEL (solid line) and EEG (dashed line) point spectra, evaluated in the narrow-beam limit, at impact parameter $\mathbf{R}_0 = (1/\sqrt{2})(40 \text{ nm}, 40 \text{ nm})$. The optical polarization is $\hat{\boldsymbol{\epsilon}} = \hat{\mathbf{x}}$ in the laser-stimulated EEG calculations. Gray and magenta colors correspond to $\hat{\boldsymbol{\mathcal{J}}}_{fi}$ along $\hat{\mathbf{z}}$ and $\hat{\mathbf{x}}$, respectively. (b) Phase-shaped EEL spectrum images at the dipole LSP resonance energy of 3.4 eV. Each column corresponds to the labeled $\hat{\boldsymbol{\mathcal{J}}}_{fi}$. (c) Phase-shaped EEG spectrum images at 3.4 eV. The optical excitation polarization state $\hat{\boldsymbol{\epsilon}}$ varies between rows, while each column corresponds to the labeled $\hat{\boldsymbol{\mathcal{J}}}_{fi}$. For $\hat{\boldsymbol{\epsilon}} = \{\hat{\mathbf{x}}, \hat{\mathbf{L}}\}$, the optical axis is chosen to be along $\hat{\mathbf{z}}$, while for $\hat{\boldsymbol{\epsilon}} = \hat{\mathbf{z}}$ it is chosen to be along $\hat{\mathbf{x}}$. Panels with $\hat{\boldsymbol{\mathcal{J}}}_{fi} = \{\hat{\mathbf{x}}, \hat{\mathbf{y}}, \hat{\mathbf{L}}\}$ and with $\hat{\boldsymbol{\epsilon}} = \{\hat{\mathbf{x}}, \hat{\mathbf{L}}\}$ share a common scale, while panels with $\hat{\boldsymbol{\mathcal{J}}}_{fi} = \hat{\mathbf{z}}$ are separately scaled. The incident velocity of the probing electron is $\mathbf{v}_i = 0.7c\hat{\mathbf{z}}$ in all cases.

as seen in Fig. 4(a), the dipolar localized surface plasmon (LSP) is clearly evident near 3.4 eV. Here it is apparent that both transitions with $\hat{\boldsymbol{\mathcal{J}}}_{fi}$ oriented parallel and perpendicular to the electron trajectory couple to the quadrupolar LSP mode near 3.6 eV, albeit with different strengths. The EEG spectra,

meanwhile, are dominated by the optically bright dipolar response of the sphere, whereas the higher-order dark modes are inaccessible by the stimulating optical pump field.

The EEL spectrum images obtained by plotting $\Gamma_{fi}^{\text{loss}}(\mathbf{R}_0, \omega)$ as a function of the impact parameter $\mathbf{R}_0$ at the dipole LSP energy 3.4 eV are shown in Fig. 4(b). In the conventional EEL case, where $\hat{\boldsymbol{\mathcal{J}}}_{fi}^{\perp} = \mathbf{0}$ resulting in $\hat{\boldsymbol{\mathcal{J}}}_{fi} = \hat{\boldsymbol{\mathcal{J}}}_{fi}^{\parallel} = \hat{\mathbf{z}}$ (gray, left), the spectrum image exhibits the expected circular symmetry. Meanwhile, when $\hat{\boldsymbol{\mathcal{J}}}_{fi}^{\perp} \neq \mathbf{0}$, producing a $\hat{\boldsymbol{\mathcal{J}}}_{fi}^{\perp}$ oriented along $\hat{\mathbf{x}}$ ($\hat{\mathbf{y}}$) and outlined in magenta (green), the spectrum image shows slight elongation in the direction of the transition current density. As required by symmetry, the circularly polarized $\hat{\boldsymbol{\mathcal{J}}}_{fi}^{\perp} = \hat{\mathbf{L}}$ (red) couples with radial symmetry to the spherical target. In Fig. 4(b) the $\hat{\boldsymbol{\mathcal{J}}}_{fi}^{\parallel} = \hat{\mathbf{z}}$ plot is normalized to a maximum of 10^{-2} eV^{-1}, while the $\hat{\boldsymbol{\mathcal{J}}}_{fi}^{\perp} \in \{\hat{\mathbf{x}}, \hat{\mathbf{y}}, \hat{\mathbf{L}}\}$ cases share a common normalization factor of 10^{-8} eV^{-1} for a beam waist of 1 nm. The small perpendicular to parallel ratio of signals represents a hurdle to phase-shaped EEL spectroscopy measurements regarding limits of detection, although measurements of this type have been achieved previously [61]. Phase-shaped EEG spectrum images at the same dipole LSP energy 3.4 eV are presented in Fig. 4(c). The optical excitation polarization state $\hat{\boldsymbol{\epsilon}}$ varies between rows, while each column corresponds to the labeled component of $\hat{\boldsymbol{\mathcal{J}}}_{fi}$. For $\hat{\boldsymbol{\epsilon}} = \{\hat{\mathbf{x}}, \hat{\mathbf{L}}\}$, the optical axis is chosen to be along $\hat{\mathbf{z}}$. There $\hat{\boldsymbol{\mathcal{J}}}_{fi}^{\perp} = \hat{\mathbf{x}}$, $\hat{\mathbf{y}}$, and $\hat{\mathbf{L}}$ share a common scale factor, while $\hat{\boldsymbol{\mathcal{J}}}_{fi} = \hat{\mathbf{z}}$ is separately scaled. The ratio of the transverse to longitudinal EEG probabilities is $\Gamma_{fi\perp}^{\text{gain}}/\Gamma_{fi\parallel}^{\text{gain}} \approx 10^{-5}$ for a 200-keV electron beam with a waist of 1 nm. These findings are consistent with earlier theoretical [66] and experimental [101] studies. For the $\hat{\boldsymbol{\epsilon}} = \hat{\mathbf{z}}$ case, the optical axis is chosen to be along $\hat{\mathbf{x}}$ and the ratio of transverse to longitudinal EEG signals remains similarly small (approximately 10^{-5}), but all signals are smaller by approximately 10^{-3} in this excitation geometry. Comparison of Figs. 4(b) and 4(c) highlights the differing identities of the excitation sources and roles played by $\mathbf{J}_{fi}$ in EEL and laser-stimulated EEG processes. When considering EEL events, the STEM electron acts as both a spatially dependent pump and probe sourced by the transition current density $\mathbf{J}_{fi}(\mathbf{R}_0)$ at impact parameter $\mathbf{R}_0$. In stark contrast, as alluded to in Sec. II, the pump and the probe are decoupled for laser-stimulated EEG processes. Specifically, as seen in Eq. (11), the pump is the optical source exciting the target's induced field $\mathbf{E}_{\nu}^{(+)}$, which is then probed by the electron's transition current density $\mathbf{J}_{fi}(\mathbf{R}_0)$ at $\mathbf{R}_0$.

B. Numerical evaluation of the inelastic double-differential cross section

From Eqs. (39) and (43), the wide-field inelastic DDCS can be expressed as

$$\frac{\partial^2 \sigma}{\partial E_{if} \partial \Omega_f} = -\frac{m^2 L^6}{(2\pi)^3 \hbar^3}\left(\frac{k_f}{k_i}\right)\int d\omega\, w_{fi}^{\text{loss}}(\omega) = -\frac{1}{4\pi^3}\frac{k_f}{k_i}\left(\frac{v_i m L^2}{\hbar^2}\right)^2 \text{Im}\left(\sum_j \mathbf{E}_{fi}^{0*}(\mathbf{x}_j, \omega = \varepsilon_{if})\cdot\mathbf{p}_j(\omega = \varepsilon_{if})\right). \quad (46)$$
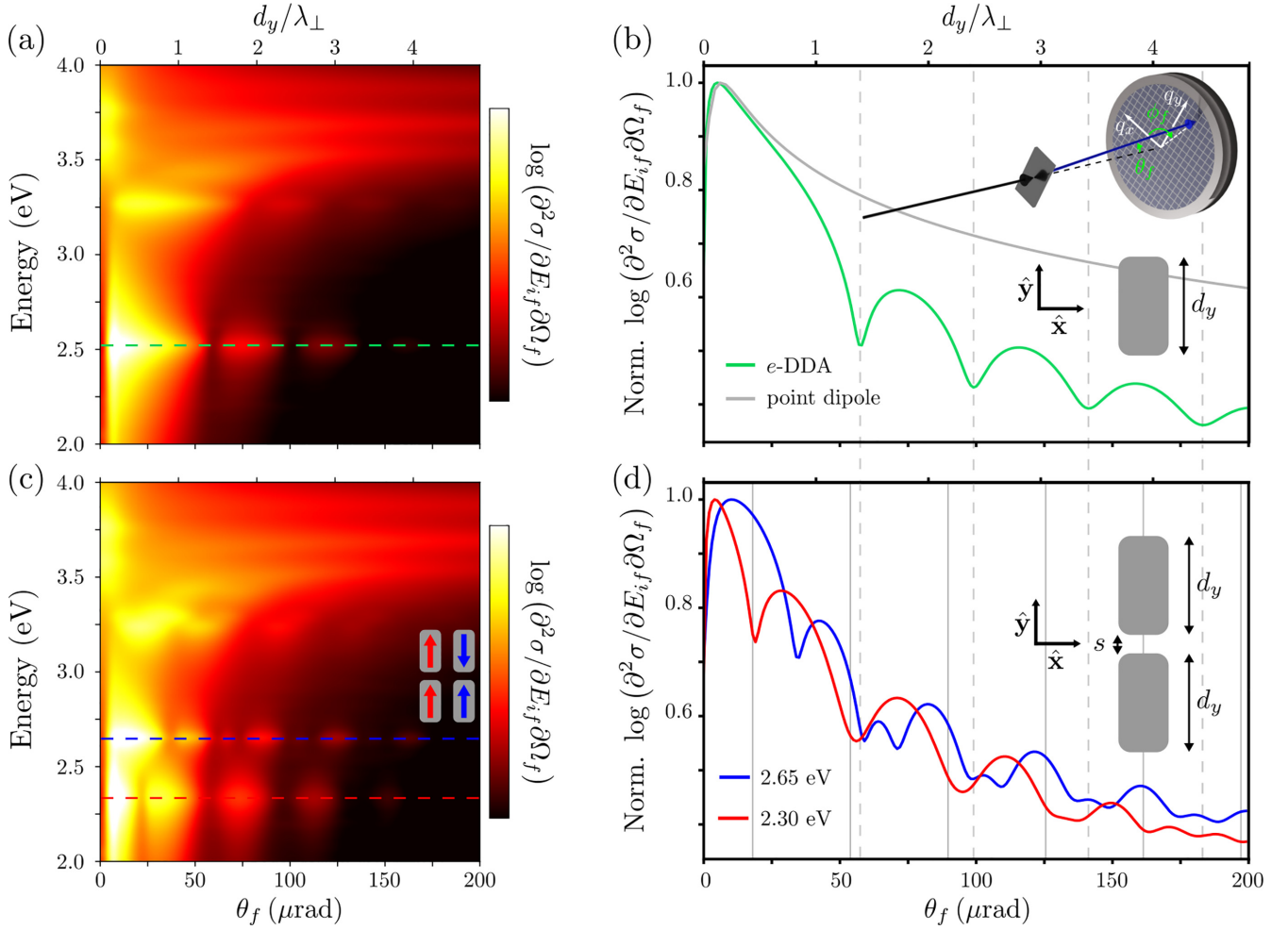
FIG. 5. DDCSs for plasmonic nanorod monomer and dimer systems evaluated using the e-DDA. (a) Numerically calculated DDCS (logarithmic scale) for a silver nanorod with Cartesian dimensions of $30 \times 60 \times 15$ nm^3. The incident electron is directed along $\hat{\mathbf{z}}$ with 200 keV kinetic energy and the collected scattering direction is varied from $\theta_f = 0$ μrad (along $\hat{\mathbf{z}}$) to $\theta_f = 200$ μrad, with $\phi_f = \pi/2$ fixed such that $\mathbf{q}_\perp = q_\perp \hat{\mathbf{y}}$. The quantity $d/\lambda_\perp$ (upper horizontal axis) is the rod length (60 nm) along the momentum recoil direction divided by the transverse recoil wavelength $\lambda_\perp = 2\pi/q_\perp$. (b) Lineout of the DDCS in (a) at 2.5 eV (green line). The gray trace is the DDCS of an anisotropic point dipole evaluated using the analytic expression in Eq. (40). Vertical gray dashed lines indicate single-particle diffraction minima. Insets show schematic depictions of the scattering and target geometries. (c) Same as (a) but for a homodimer target composed of two copies of the nanostructure considered in (a) and (b) arranged tip-to-tip along the y axis with an $s = 10$ nm gap. (d) Lineouts from (c) at 2.30 eV (red line) and 2.65 eV (blue line). Vertical gray dashed lines indicate single-slit-diffraction minima, while gray solid lines denote double-slit-interference minima at 2.30 eV. All panels use the base 10 logarithm to scale the DDCS.

We have implemented within the e-DDA the plane-wave transition fields defined in Eqs. (A4) and (A6) in the Appendix, sourced by the transition currents (18) and (19), respectively, for the cases of scattering from either a single or a coherent superposition of two incident plane waves to a single outgoing plane-wave state.

The DDCSs for inelastic scattering of wide-field plane-wave electron states from plasmonic nanorod monomers and dimers are presented in Fig. 5. Probing electrons have an initial kinetic energy of 200 keV and wave vector directed along the TEM axis, i.e., $\hat{\mathbf{k}}_i = \hat{\mathbf{z}}$, while the outgoing wave vectors $\mathbf{k}_f$ possess a nonzero y component such that the transverse momentum recoil $\hbar\mathbf{q}_\perp$ is along $\hat{\mathbf{y}}$. Working in the low-loss-energy regime in order to observe the plasmonic modes of interest, Fig. 5(a) shows the calculated DDCS (logarithmic scale) for an anisotropic silver rod with Cartesian dimensions of

$30 \times 60 \times 15$ nm^3 (width, length, and height) as a function of scattering angle θ_f and loss energy. The nanorod is orientated with its longest dimension d_y along in direction of collected transverse recoils ($\phi_f = \pi/2$), leading to the lowest-energy long-axis dipole mode near 2.50 eV dominating the DDCS. Since the transversely polarized components of the transition field $\mathbf{E}^0_{fi}$ in Eq. (A4) are proportional to $\mathbf{q}_\perp$, transversely oriented LSP modes of the nanorod do not contribute to the DDCS at $\theta_f = 0$ μrad. The apparent features at $\theta_f = 0$ μrad and energies above 3.50 eV in Fig. 5(a) arise from longitudinal multipoles oriented along $\hat{\mathbf{z}}$.

Figure 5(b) shows a lineout from Fig. 5(a) at the long-axis dipole LSP energy marked by the green dashed line. The gray trace in Fig. 5(b) is calculated using the analytic form of the DDCS given in Eq. (40) for a single-point dipole representing the target. The anisotropy of the

nanorod response is captured by detuning the shorter-axis dipole LSP energies above 2.50 eV in the dipole's effective polarizability. As a consequence, $\partial^2\sigma/\partial E_{if}\partial\Omega_f \propto |\mathbf{E}_{fi}^0 \cdot \hat{\mathbf{y}}|^2$, which ensures $\partial^2\sigma/\partial E_{if}\partial\Omega_f|_{\theta_f=0} = 0$. At moderate opening angles (greater than approximately 5 μrad) the DDCS decreases as the opening angle increases, which starting from Eq. (A4) and $Q_\parallel \gg |\mathbf{Q}_\perp| = |\mathbf{q}_\perp|$ can be shown by $\mathbf{E}_{fi}^0 \cdot \hat{\mathbf{y}} \propto Q_\parallel q_\parallel \mathbf{q}_\perp \cdot \hat{\mathbf{y}}/(\mathbf{q}_\perp^2 + q_\parallel^2 - \omega^2/c^2) = Q_\parallel q_\parallel |\mathbf{k}_f| \sin\theta_f/[|\mathbf{k}_f|^2 \sin^2\theta_f + \omega^2(1/v_i^2 - 1/c^2)]$. For a 200-keV electron with loss energy $\hbar\epsilon_{if} = 2.5$ eV, $|\mathbf{k}_f|\sin\theta_f \gtrsim \omega/\gamma_i v_i$ at opening angles greater than 5 μrad, leading to $\partial^2\sigma/\partial E_{if} d\Omega_f \propto 1/\sin^2\theta_f$. This effect exists independent of the target geometry and represents the decreasing probability of low-loss events with moderate transverse recoil. Separately the lineouts in θ_f on the order of the 5-μrad range are primarily dictated by the growing in of the transverse LSP mode, as at smaller angles $\mathbf{E}_{fi}^0 \cdot \hat{\mathbf{y}} \propto \mathbf{q} \cdot \hat{\mathbf{y}} = |\mathbf{k}_f|\sin\theta_f$ and the lineout is taken at the $\hat{\mathbf{y}}$-oriented dipole mode energy. Unlike in the narrow-beam limit, the DDCS observable has equal magnitude contributions from transverse and longitudinal recoils, which is a well-known experimental and theoretical result of EEL DDCS on an anisotropic target [89,102]. In addition to tracking the angular scattering behavior predicted by the point dipole model at small scattering angles (less than approximately 25 μrad), the lineout shown in green exhibits a progression of diffraction maxima and minima with increasing θ_f arising from the finite extent of the target. The single-particle diffraction minima, indicated by vertical gray dashed lines, are located nearby angles θ_m corresponding to single-slit diffraction minima predicted using $d_y \sin\theta_m = m\lambda_e$, where integers m index the diffraction minima and λ_e is the de Broglie wavelength of the electron.

Figures 5(c) and 5(d) consider a nanorod dimer consisting of a pair of the silver rods from Figs. 5(a) and 5(b) displaced along $\hat{\mathbf{y}}$ such that there is an $s = 10$ nm gap between the rod tips. The dimer's DDCS is presented in Fig. 5(c), where the bonding (red) and antibonding (blue) hybridized long-axis dipole LSP modes are visible at energies slightly below and above 2.5 eV, respectively. Lineouts from Fig. 5(c) at loss energies corresponding to the bonding and antibonding dimer modes are shown in Fig. 5(d), again displaying multiple diffraction minima and maxima. In analogy to the double-slit experiment, each nanorod is a source of single-particle diffraction in addition to matter-wave interference arising from the $d_\perp + s = 70$ nm center-to-center displacement of the the nanorods. For example, each DDCS minimum observed at the bonding mode energy (2.30 eV) occurs at an angle corresponding to either one of the single-particle diffraction minima from Fig. 5(b) marked by vertical gray dashed lines or at angles θ_n satisfying the double-slit interference condition $n\lambda_\perp = d_y + s$, which are indicated by vertical gray solid lines. The condition for constructive interference at the antibonding resonance energy is $(n + 1/2)\lambda_\perp = d_y + s$.

An investigation of inelastic scattering involving superposition plane-wave electron states interacting with a chiral nanophotonic target is presented in Fig. 6. Specifically, the target is the well-understood Born-Kuhn (BK) structure [103], composed of two gold nanorods arranged in an L shape with a relative displacement ζ between the rods centered
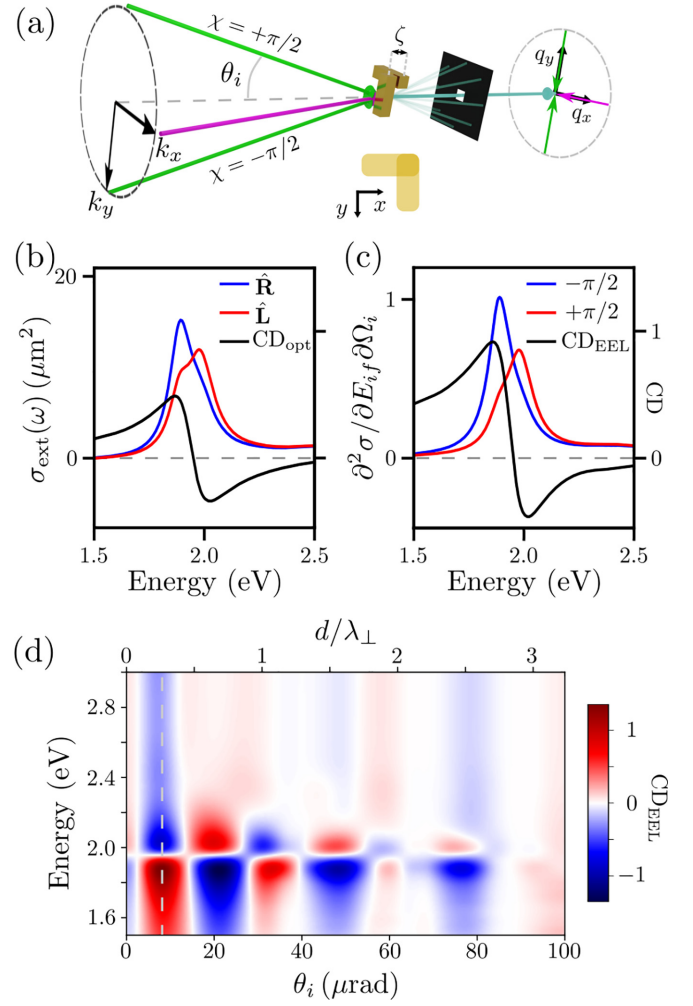
FIG. 6. Numerical evaluation of the circular dichroic response of a chiral nanorod structure probed using wide-field EEL spectroscopy within the *e*-DDA. (a) Scheme showing the gold nanorod BK structure and probing geometries. Superposition plane-wave electron states are incident from the left, while an aperture (black) postselects the outgoing electron state along the TEM ($\hat{\mathbf{z}}$) axis. (b) Optical extinction spectra for incident plane-wave wave vectors along $\hat{\mathbf{z}}$ with circular polarization states $\hat{\boldsymbol{\epsilon}} = \hat{\mathbf{R}}$ (blue) and $\hat{\mathbf{L}}$ (red). The optical circular dichroism $\mathrm{CD}_{\mathrm{opt}}$ is shown in black and shares its secondary y axis with (c). (c) DDCS spectra of the same BK structure for superposition plane-wave electron states with $\chi = +\pi/2$ (red) and $\chi = -\pi/2$ (blue). The $\mathrm{CD}_{\mathrm{EEL}}$ spectrum is shown in black. (d) Angle-θ_i-resolved $\mathrm{CD}_{\mathrm{EEL}}$ spectra. The gray dashed line indicates the fixed angle of the lineouts in (c). The incident electron kinetic energy in (c) and (d) is 200 keV.

along $\hat{\mathbf{z}}$, as demonstrated in Fig. 6(a). Here the long and short axes of each nanorod are 100 nm and 30 nm, respectively, $\zeta = 40$ nm, and tabulated gold dielectric data are taken from the literature [100]. Figure 6(b) shows the optical extinction spectra of the BK target for incident wave vectors along $\hat{\mathbf{z}}$ and polarizations $\hat{\boldsymbol{\epsilon}} = \hat{\mathbf{L}}$ (red) and $\hat{\mathbf{R}}$ (blue). As is well understood (see the Appendix) [104,105], both incident field helicities couple, albeit with unequal strengths, to the bonding and antibonding LSP modes near 2.0 eV involving the long-axis dipoles. The optical circular dichroism

$\text{CD}_{\text{opt}} = 2(\sigma_{\text{ext}}^{\hat{\mathbf{R}}} - \sigma_{\text{ext}}^{\hat{\mathbf{L}}})/(\sigma_{\text{ext}}^{\hat{\mathbf{R}}} + \sigma_{\text{ext}}^{\hat{\mathbf{L}}})$ spectrum is shown in black, which exhibits the BK system's chiral response and serves as a point of comparison against the electron-based observables.

As depicted in Fig. 6(a), free-electron plane-wave superposition states $\psi_{k_x k_y}^{\chi}(x, y, z)$ are incident from the left, while an aperture situated in the diffraction plane postselects the outgoing free electrons along the TEM axis with $\mathbf{k}_{\perp}^f = \mathbf{0}$, i.e., $\psi_{k_{\parallel}'}(x, y, z)$. It has been shown previously that the response of targets as measured by wide-field EEL spectroscopy with pre- and postselection of such states with $k_x = k_y$ and $\chi = \pm\pi/2$ in many ways mimics the optical response under circularly polarized optical excitation [37,38,67]. Indeed, Fig. 6(c) presents DDCS spectra of the BK target for $\psi_{k_x k_y}^{\chi}(x, y, z) \rightarrow \psi_{k_{\parallel}'}(x, y, z)$, producing the transition current density given by Eq. (19), for the scenarios of $\chi = \pm\pi/2$. The circular dichroism CD_{EEL} (black) is again defined as twice the difference in the $\chi = \pm\pi/2$ DDCS spectra normalized by the sum and strongly resembles the CD_{opt} spectrum in Fig. 6(b). Figure 6(c) presents the CD_{EEL} spectra as a function of convergence angle θ_i. Like the nanorod dimer presented in Fig. 5, the BK system exhibits both single-slit diffraction and double-slit interference effects [Fig. 6(d)], though the superposition state excitation and BK target geometry conspire to produce more complicated beating patterns than those observed in Fig. 5(c). The vertical gray dashed line in Fig. 6(d) indicates the convergence angle θ_i of the spectra presented in Fig. 6(c).

VII. CONCLUSION

Development of capabilities to prepare, parse, and measure transversely phase-structured electron states in the electron microscope has created the opportunity for state- and energy-resolved inelastic-scattering observables, adding to the rapidly evolving toolkit used to interrogate nanoscale systems in the low-loss regime. Here we presented general expressions for transversely phase-shaped EEL and continuous-wave laser-stimulated EEG spectroscopies for transversely localized vortex and nonvortex electron states, and the DDCS for wide-field electron plane waves under minimal assumptions regarding the magnitudes of electron velocity and energy exchange. By exploiting a quantum-mechanical treatment that accounts explicitly for the transverse degrees of freedom

of the probing electron wave functions, we showcased the ability to retrieve information about the optical near-field and electromagnetic response of nanophotonic targets using inelastic scattering of phase-shaped free electrons following energy-momentum postselection. A numerical procedure for evaluating derived observables was presented that allows for flexibility regarding particle number, size, geometry, and material composition. Example calculations for several prototypical plasmonic monomer and dimer systems were investigated to highlight the utility of our approach to analyze mode symmetries, local response field characteristics, chiral responses, and matter-wave diffraction phenomena. The general procedures outlined for constructing wide-field plane-wave and nondiffracting twisted and nontwisted electron beams with distinct transverse polarization and topological textures, in addition to the state- and energy-resolved observables, can be readily applied to many areas of atomic, molecular, and materials physics. In particular, we have drawn attention to an application of free-electron qubits, whereby transitions between different OAM qubit states produce transition current densities with unique polarization and vector profiles, including analogs of optical polarization states and other more general forms of structured light. The theoretical framework presented can be extended to describe beam coherence in electron holography [106,107] via a density-matrix formalism [108] and utilized to explore the role of pure and mixed electron states in inelastic scattering and the concurrent transfer of quantum information in the form of quantized energy and OAM [54,56,57,109]. Furthermore, the use of transversely phase-structured free-electron states realizable in TEMs, STEMs, and ultrafast TEMs can lead to additional manifestations of unique electromagnetic fields [27,28] and electron paraxial skyrmionic beams [29], all of which could play vital roles in the investigation of novel optically forbidden atomic, molecular, material, and topological excitations [30,110–113].

APPENDIX

1. Vacuum transition vector potentials and electric fields

The transition vector potentials and electric fields associated with each of the transition current densities in Sec. IV are presented below. Specifically, the vacuum electric field

$$\mathbf{E}_{fi}^0(\mathbf{x}, \omega) = \frac{ic}{\omega}\left[\left(\frac{\omega}{c}\right)^2 \overset{\leftrightarrow}{\mathbf{I}} + \boldsymbol{\nabla}\boldsymbol{\nabla}\right] \cdot \mathbf{A}_{fi}^0(\mathbf{x}, \omega)$$

$$= \frac{i}{\omega} \int d\mathbf{x}' \left[\left(\frac{\omega}{c}\right)^2 \overset{\leftrightarrow}{\mathbf{I}} + \boldsymbol{\nabla}\boldsymbol{\nabla}\right] \frac{e^{i(\omega/c)|\mathbf{x}-\mathbf{x}'|}}{|\mathbf{x} - \mathbf{x}'|} \left(\frac{L}{v_i}\right)\mathbf{J}_{fi}(\mathbf{x}')$$

$$= -4\pi i\omega \int d\mathbf{x}' \overset{\leftrightarrow}{\mathbf{G}}{}^0(\mathbf{x}, \mathbf{x}', \omega) \cdot \left(\frac{L}{v_i}\right)\mathbf{J}_{fi}(\mathbf{x}') \tag{A1}$$

plays an important role in the observable EEL and EEG processes and depends upon the vector potential

$$\mathbf{A}_{fi}^0(\mathbf{x}, \omega) = \frac{1}{c} \int d\mathbf{x}' \frac{e^{i(\omega/c)|\mathbf{x}-\mathbf{x}'|}}{|\mathbf{x}-\mathbf{x}'|} \left(\frac{L}{v_i}\right) \mathbf{J}_{fi}(\mathbf{x}'),\tag{A2}$$

presented here in the Lorenz gauge. Beginning with the transition current density in Eq. (18) associated with the transition between single-plane-wave states $\psi_{\mathbf{k}_i}(x, y, z)$ and $\psi_{\mathbf{k}_f}(x, y, z)$, where $\mathbf{k}_i$ and $\mathbf{k}_f$ are arbitrary wave vectors, the vacuum vector potential

$$\mathbf{A}_{\mathbf{k}_f \mathbf{k}_i}^0(\mathbf{x}, \omega) = \frac{2\pi e\hbar}{mcv_i L^2} \frac{e^{i\mathbf{q}\cdot\mathbf{x}}}{(\omega/c)^2 - q^2} \mathbf{Q} \tag{A3}$$

and electric field

$$\mathbf{E}_{\mathbf{k}_f \mathbf{k}_i}^0(\mathbf{x}, \omega) = \frac{2\pi i e\gamma_i}{k_i L^2 \omega} \frac{e^{i\mathbf{q}\cdot\mathbf{x}}}{(\omega/c)^2 - q^2} \left[\left(\frac{\omega}{c}\right)^2 \overset{\leftrightarrow}{\mathbf{I}} - \mathbf{q}\mathbf{q}\right] \cdot \mathbf{Q} \tag{A4}$$

are readily obtained upon using the integral identity $\int d\mathbf{x}' e^{i(\omega/c)|\mathbf{x}-\mathbf{x}'|} e^{\mp i\mathbf{q}\cdot\mathbf{x}'}/|\mathbf{x}-\mathbf{x}'| = -4\pi e^{\mp i\mathbf{q}\cdot\mathbf{x}}/[(\omega/c)^2 - q^2]$.

The vacuum transition vector potential sourced by the superposition plane-wave state transition current density in Eq. (19) takes the form

$$\mathbf{A}_{k_\parallel', k_x k_y}^{\chi 0}(\mathbf{x}, \omega) = \frac{2\pi e\hbar}{\sqrt{2}mcv_i L^2} e^{iq_\parallel z}\left[\frac{k_x e^{ik_x x}}{(\omega/c)^2 - k_x^2 - q_\parallel^2}\hat{\mathbf{x}} + \frac{k_y e^{i\chi} e^{ik_y y}}{(\omega/c)^2 - k_y^2 - q_\parallel^2}\hat{\mathbf{y}} + Q_\parallel\left(\frac{e^{ik_x x}}{(\omega/c)^2 - k_x^2 - q_\parallel^2} + \frac{e^{i\chi} e^{ik_y y}}{(\omega/c)^2 - k_y^2 - q_\parallel^2}\right)\hat{\mathbf{z}}\right]\tag{A5}$$

for the superposition state $\psi_{k_x k_y}^\chi(x, y, z) = (1/\sqrt{2L})[\Psi_{k_x}(x, y) + \Psi_{k_y}(x, y)e^{i\chi}]e^{ik_\parallel z}$ introduced in Sec. III, transitioning to the final pinhole state $\psi_{k_\parallel'}(x, y, z) = L^{-3/2}e^{ik_\parallel' z}$ oriented along the TEM ($\hat{\mathbf{z}}$) axis. Associated with this vector potential is the superposition plane-wave state transition electric field

$$\mathbf{E}_{k_\parallel', k_x k_y}^{\chi 0}(\mathbf{x}, \omega) = \frac{-2\pi i e\hbar}{\sqrt{2}m\omega L^2 v_i}\left[\frac{k_x^2 + Q_\parallel q_\parallel - \left(\frac{\omega}{c}\right)^2}{k_x^2 + q_\parallel^2 - \left(\frac{\omega}{c}\right)^2}k_x e^{ik_x x}\hat{\mathbf{x}} + \frac{k_y^2 + Q_\parallel q_\parallel - \left(\frac{\omega}{c}\right)^2}{k_y^2 + q_\parallel^2 - \left(\frac{\omega}{c}\right)^2}k_y e^{ik_y y}e^{i\chi}\hat{\mathbf{y}}\right.$$
$$\left. + \left(\frac{k_x^2 q_\parallel + Q_\parallel q_\parallel^2 - Q_\parallel\left(\frac{\omega}{c}\right)^2}{k_x^2 + q_\parallel^2 - \left(\frac{\omega}{c}\right)^2}e^{ik_x x} + \frac{k_y^2 q_\parallel + Q_\parallel q_\parallel^2 - Q_\parallel\left(\frac{\omega}{c}\right)^2}{k_y^2 + q_\parallel^2 - \left(\frac{\omega}{c}\right)^2}e^{ik_y y}e^{i\chi}\right)\hat{\mathbf{z}}\right]e^{iq_\parallel z},\tag{A6}$$

where $\mathbf{Q} = \mathbf{k}_i + \mathbf{k}_f$ and $\mathbf{q} = \mathbf{k}_i - \mathbf{k}_f$ are the same total and recoil wave vectors defined previously.

In the case of focused beams, more specifically in the small-beamwidth limit, we present only the vacuum transition fields involving one unit of OAM exchange between initial and final electron-scattering states. The narrow-beam limit, whereby the transverse electron wave function reduces to the transverse δ function [51], is adopted in all expressions. The transition vector potential and electric field associated with the HG transition current density in Eq. (23) describing the scattering from $\psi_{10}(x, y, z)$ to $\psi_{00}(x, y, z)$ are

$$\mathbf{A}_{00,10}^0(\mathbf{x}, \omega) = -\frac{2ie\hbar}{mv_i cw_0}\left[K_0\left(\frac{q_\parallel \Delta R_0}{\gamma_i}\right)\hat{\mathbf{x}} + i\frac{q_\parallel Q_\parallel w_0^2}{4\gamma_i}\frac{\Delta x}{\Delta R_0}K_1\left(\frac{q_\parallel \Delta R_0}{\gamma_i}\right)\hat{\mathbf{z}}\right]e^{iq_\parallel z}\tag{A7}$$

and

$$\mathbf{E}_{00,10}^0(\mathbf{x}, \omega) = \frac{2\hbar e}{mw_0\omega v_i}\left[\frac{\omega^2}{c^2}\overset{\leftrightarrow}{\mathbf{I}} + \nabla\nabla\right] \cdot \left[K_0\left(\frac{q_\parallel \Delta R_0}{\gamma_i}\right)\hat{\mathbf{x}} + i\frac{q_\parallel Q_\parallel w_0^2}{4\gamma_i}\frac{\Delta x}{\Delta R_0}K_1\left(\frac{q_\parallel \Delta R_0}{\gamma_i}\right)\hat{\mathbf{z}}\right]e^{iq_\parallel z}$$
$$= \frac{\hbar e}{2mw_0\omega v_i}\left\{\left[\left(\frac{4\omega^2}{c^2} + \frac{q_\parallel^2}{\gamma_i^2}\left(4 + q_\parallel Q_\parallel w_0^2\right)\frac{\Delta x^2}{\Delta R_0^2}\right)K_0\left(\frac{q_\parallel \Delta R_0}{\gamma_i}\right) + \frac{q_\parallel}{\gamma_i}\left(4 + q_\parallel Q_\parallel w_0^2\right)\frac{(\Delta x^2 - \Delta y^2)}{\Delta R_0^3}K_1\left(\frac{q_\parallel \Delta R_0}{\gamma_i}\right)\right]\hat{\mathbf{x}}\right.$$
$$\left. + \frac{q_\parallel^2}{\gamma_i^2}\left(4 + q_\parallel Q_\parallel w_0^2\right)\frac{\Delta x\Delta y}{\Delta R_0^2}K_2\left(\frac{q_\parallel \Delta R_0}{\gamma_i}\right)\hat{\mathbf{y}} + \frac{i}{\gamma_i}\frac{\Delta x}{\Delta R_0}\left(q_\parallel Q_\parallel w_0^2\frac{\omega^2}{c^2} - q_\parallel^2\left(1 + q_\parallel Q_\parallel w_0^2\right)\right)K_1\left(\frac{q_\parallel \Delta R_0}{\gamma_i}\right)\hat{\mathbf{z}}\right\}e^{iq_\parallel z},\tag{A8}$$

respectively, where $\Delta R_0 = |\mathbf{R} - \mathbf{R}_0|$, $\Delta x = |x - x_0|$, and $\Delta y = |y - y_0|$. By symmetry, scattering from HG $\psi_{01}(x, y, z)$ to $\psi_{00}(x, y, z)$ can be obtained from Eqs. (A7) and by (A8) interchanging $\hat{\mathbf{x}}$ with $\hat{\mathbf{y}}$, resulting in $\mathbf{A}_{00,01}^0(\mathbf{x}, \omega)$ and $\mathbf{E}_{00,01}^0(\mathbf{x}, \omega)$. If the transverse state does not change in the scattering process, as is the case in the conventional EEL signal, the vacuum vector potential and electric field associated with the current density in Eq. (24) where $n' = n = 0$ and $m' = m = 0$ become

$$\mathbf{A}_{00,00}^0(\mathbf{x}, \omega) = \left(\frac{\hbar e}{mv_i c}\right)Q_\parallel K_0\left(\frac{q_\parallel \Delta R_0}{\gamma_i}\right)\hat{\mathbf{z}}e^{iq_\parallel z}\tag{A9}$$

and

$$\mathbf{E}^0_{00,00}(\mathbf{x}, \omega) = \frac{\hbar e}{\omega m v_i} Q_\parallel \left[\frac{q_\parallel^2}{\gamma_i \Delta R_0} K_1 \left(\frac{q_\parallel \Delta R_0}{\gamma} \right) (\Delta x \hat{\mathbf{x}} + \Delta y \hat{\mathbf{y}}) + i \left(\frac{\omega^2}{c^2} - q_\parallel^2 \right) K_0 \left(\frac{q_\parallel \Delta R_0}{\gamma} \right) \hat{\mathbf{z}} \right] e^{iq_\parallel z}. \tag{A10}$$

The latter is the well-known classical field of a uniformly moving point electron [51,69] in the nonrecoil approximation where $q_\parallel = \omega/v_i$ and $Q_\parallel = 2k_\parallel^i$.

Transitions between LG states $\psi_{\ell p}(\rho, \phi, z)$ and $\psi_{\ell' p'}(\rho, \phi, z)$ involving one unit of OAM can be derived from the above HG transitions by linear combination. Specifically,

$$\mathbf{A}^0_{\ell'=0,p'=0,\ell=\pm1,p=0}(\rho, \phi, z, \omega) = \frac{1}{\sqrt{2}} \left[\mathbf{A}^0_{00,10}(\mathbf{x}, \omega) \pm i \mathbf{A}^0_{00,01}(\mathbf{x}, \omega) \right] \tag{A11}$$

and

$$\mathbf{E}^0_{\ell'=0,p'=0,\ell=\pm1,p=0}(\rho, \phi, z, \omega) = \frac{1}{\sqrt{2}} \left[\mathbf{E}^0_{00,10}(\mathbf{x}, \omega) \pm i \mathbf{E}^0_{00,01}(\mathbf{x}, \omega) \right]. \tag{A12}$$

All electric fields introduced in the Appendix are coded within the *e*-DDA and can be used to calculate the presented EEL observables in both wide-field and focused-beam limits.

2. Observables under interchange of initial and final states

The EEL rate w_{fi} is proportional to $\int d\mathbf{x} \, d\mathbf{x}' \mathbf{J}^*_{fi}(\mathbf{x}) \cdot \overleftrightarrow{\mathbf{G}}(\mathbf{x}, \mathbf{x}', \omega) \cdot \mathbf{J}_{fi}(\mathbf{x}')$. By interchanging the 3D coordinates $\mathbf{x}$ and $\mathbf{x}'$ and invoking reciprocity, i.e., $G_{\alpha\beta}(\mathbf{x}, \mathbf{x}', \omega) = G_{\beta\alpha}(\mathbf{x}', \mathbf{x}, \omega)$,

$$\int d\mathbf{x} \, d\mathbf{x}' [\mathbf{J}_{fi}(\mathbf{R}) e^{iq_\parallel z}]^*_\alpha G_{\alpha\beta}(\mathbf{x}, \mathbf{x}', \omega) [\mathbf{J}_{fi}(\mathbf{R}') e^{iq_\parallel z'}]_\beta = \int d\mathbf{x} \, d\mathbf{x}' [\mathbf{J}_{fi}(\mathbf{R})]^*_\alpha G_{\alpha\beta}(\mathbf{x}, \mathbf{x}', \omega) [\mathbf{J}_{fi}(\mathbf{R}')]_\beta e^{-iq_\parallel(z-z')}$$

$$= \int d\mathbf{x} \, d\mathbf{x}' [\mathbf{J}_{if}(\mathbf{R})]_\alpha G_{\alpha\beta}(\mathbf{x}, \mathbf{x}', \omega) [\mathbf{J}_{if}(\mathbf{R}')]^*_\beta e^{-iq_\parallel(z-z')}$$

$$= \int d\mathbf{x} \, d\mathbf{x}' [\mathbf{J}_{if}(\mathbf{R}')]^*_\beta G_{\beta\alpha}(\mathbf{x}', \mathbf{x}, \omega) [\mathbf{J}_{if}(\mathbf{R})]_\alpha e^{-iq_\parallel(z-z')}$$

$$= \int d\mathbf{x} \, d\mathbf{x}' [\mathbf{J}_{if}(\mathbf{R})]^*_\alpha G_{\alpha\beta}(\mathbf{x}, \mathbf{x}', \omega) [\mathbf{J}_{if}(\mathbf{R}')]_\beta e^{-iq_\parallel(z'-z)}$$

$$= \int d\mathbf{x} \, d\mathbf{x}' [\mathbf{J}_{if}(\mathbf{R}) e^{i(-q_\parallel)z}]^*_\alpha G_{\alpha\beta}(\mathbf{x}, \mathbf{x}', \omega) [\mathbf{J}_{if}(\mathbf{R}') e^{i(-q_\parallel)z'}]_\beta, \tag{A13}$$

where $\alpha, \beta = x, y, z$ and Einstein summation notation has been used. Equation (A13) can be equivalently expressed as $w_{fi}(q_\parallel) = w_{if}(-q_\parallel)$ provided $G_{\alpha\beta}(\mathbf{x}, \mathbf{x}', \omega) = G_{\beta\alpha}(\mathbf{x}', \mathbf{x}, \omega)$. Said differently, interchanging the initial and final transverse states together with changing the sign of the recoil momentum wave vector $q_\parallel$ leaves the EEL observable invariant in a reciprocal medium. In the case of an isolated dipolar target at position $\mathbf{x}_d$ characterized by frequency-dependent polarizability $\overleftrightarrow{\boldsymbol{\alpha}}(\omega)$, $\overleftrightarrow{\mathbf{G}}(\mathbf{x}, \mathbf{x}', \omega)$ satisfies the reciprocity condition when the polarizability tensor is complex symmetric, i.e., when $\overleftrightarrow{\boldsymbol{\alpha}}(\omega) = \overleftrightarrow{\boldsymbol{\alpha}}^T(\omega)$.

3. Laser-stimulated coherent states of the target

Under the assumption that the stimulating laser field couples to a single target mode (labeled ℓ), which is driven into the coherent state $|\alpha_\ell\rangle$, the rate at which the probing electron gains energy as the target transitions to the sum of final Fock states $|n'_\ell\rangle$ is

$$w^{\text{gain}}_{fi} = \frac{2\pi}{\hbar c^2} \sum_{n'_\ell} \left| \sum_\nu \int d\mathbf{x} \, \mathbf{J}_{fi}(\mathbf{x}, t) \cdot \langle n'_\ell | \mathbf{A}^{(+)}_\nu(\mathbf{x}) a_\nu e^{-i\omega_\nu t} | \alpha_\ell \rangle \right|^2 \delta(E_f - E_i)$$

$$= \frac{2\pi}{\hbar c^2} \sum_{n'_\ell} \left| \alpha_\ell \langle n'_\ell | \alpha_\ell \rangle \int d\mathbf{x} \, \mathbf{A}^{(+)}_\ell(\mathbf{x}) \cdot \mathbf{J}_{fi}(\mathbf{x}) \right|^2 \delta(E_f - E_i). \tag{A14}$$

Coherent states can be written as $|\alpha\rangle = e^{-|\alpha|^2/2} \sum_{n=0}^{\infty} (\alpha^n/\sqrt{n!})|n\rangle$, where $|n\rangle = [(a^\dagger)^n/\sqrt{n!}]|0\rangle$. When expressed in terms of the electric field $\mathbf{E}_\ell^{(\pm)}(\mathbf{x}) = \pm(i\omega_\ell)/c\mathbf{A}_\ell^{(\pm)}(\mathbf{x})$ together with $|\langle n'_\ell|\alpha_\ell\rangle|^2 = (|\alpha_\ell|^{2n'_\ell}/n'_\ell!)e^{-|\alpha_\ell|^2}$, Eq. (A14) can be cast as

$$w_{fi}^{\text{gain}} = 2\pi \left(\frac{|\alpha_\ell|}{\hbar\omega_\ell}\right)^2 \left(\sum_{n'_\ell} \frac{|\alpha_\ell|^{2n'_\ell}}{n'_\ell!}\right) e^{-|\alpha_\ell|^2} \left|\int d\mathbf{x}\, \mathbf{E}_\ell^{(+)}(\mathbf{x}) \cdot \mathbf{J}_{fi}(\mathbf{x})\right|^2 \delta((E_f - E_i)/\hbar)$$

$$= 2\pi \left(\frac{|\alpha_\ell|}{\hbar\omega_\ell}\right)^2 \left|\int d\mathbf{x}\, \mathbf{E}_\ell^{(+)}(\mathbf{x}) \cdot \mathbf{J}_{fi}(\mathbf{x})\right|^2 \delta((E_f - E_i)/\hbar). \tag{A15}$$

[1] E. N. Lassettre, Collision cross-section studies on molecular gases and the dissociation of oxygen and water, Radiat. Res. Suppl. **1**, 530 (1959).

[2] E. N. Lassettre, M. E. Krasnow, and S. Silverman, Inelastic scattering of electrons by helium, J. Chem. Phys. **40**, 1242 (1964).

[3] J. A. Bradley, G. T. Seidler, G. Cooper, M. Vos, A. P. Hitchcock, A. P. Sorini, C. Schlimmer, and K. P. Nagle, Comparative study of the valence electronic excitations of N_2 by inelastic x-ray and electron scattering, Phys. Rev. Lett. **105**, 053202 (2010).

[4] M. Adrian, J. Dubochet, J. Lepault, and A. W. McDowall, Cryo-electron microscopy of viruses, Nature (London) **308**, 32 (1984).

[5] P. Rez, T. Aoki, K. March, D. Gur, O. L. Krivanek, N. Dellby, T. C. Lovejoy, S. G. Wolf, and H. Cohen, Damage-free vibrational spectroscopy of biological materials in the electron microscope, Nat. Commun. **7**, 10945 (2016).

[6] R. Fernandez-Leiro and S. H. W. Scheres, Unravelling biological macromolecules with cryo-electron microscopy, Nature (London) **537**, 339 (2016).

[7] J. A. Hachtel, J. Huang, I. Popovs, S. Jansone-Popova, J. K. Keum, J. Jakowski, T. C. Lovejoy, N. Dellby, O. L. Krivanek, and J. C. Idrobo, Identification of site-specific isotopic labels by vibrational spectroscopy in the electron microscope, Science **363**, 525 (2019).

[8] J. Li, J. Li, J. Tang, Z. Tao, S. Xue, J. Liu, H. Peng, X.-Q. Chen, J. Guo, and X. Zhu, Direct observation of topological phonons in graphene, Phys. Rev. Lett. **131**, 116602 (2023).

[9] C. Dwyer, T. Aoki, P. Rez, S. L. Y. Chang, T. C. Lovejoy, and O. L. Krivanek, Electron-beam mapping of vibrational modes with nanometer spatial resolution, Phys. Rev. Lett. **117**, 256101 (2016).

[10] M. J. Lagos, A. Trügler, U. Hohenester, and P. E. Batson, Mapping vibrational surface and bulk modes in a single nanocube, Nature (London) **543**, 529 (2017).

[11] R. Senga, K. Suenaga, P. Barone, S. Morishita, F. Mauri, and T. Pichler, Position and momentum mapping of vibrations in graphene nanostructures, Nature (London) **573**, 247 (2019).

[12] A. Polman, M. Kociak, and F. J. García de Abajo, Electron-beam spectroscopy for nanophotonics, Nat. Mater. **18**, 1158 (2019).

[13] Y. Auad, E. J. C. Dias, M. Tencé, J.-D. Blazit, X. Li, L. F. Zagonel, O. Stéphan, L. H. G. Tizei, F. J. García de Abajo, and M. Kociak, µeV electron spectromicroscopy using free-space light, Nat. Commun. **14**, 4442 (2023).

[14] F. Araoka, T. Verbiest, K. Clays, and A. Persoons, Interactions of twisted light with chiral molecules: An experimental investigation, Phys. Rev. A **71**, 055401 (2005).

[15] L. Allen, M. W. Beijersbergen, R. J. C. Spreeuw, and J. P. Woerdman, Orbital angular momentum of light and the transformation of Laguerre-Gaussian laser modes, Phys. Rev. A **45**, 8185 (1992).

[16] G. Molina-Terriza, J. P. Torres, and L. Torner, Twisted photons, Nat. Phys. **3**, 305 (2007).

[17] J. Harris, V. Grillo, E. Mafakheri, G. C. Gazzadi, S. Frabboni, R. W. Boyd, and E. Karimi, Structured quantum waves, Nat. Phys. **11**, 629 (2015).

[18] A. M. Yao and M. J. Padgett, Orbital angular momentum: Origins, behavior and applications, Adv. Opt. Photonics **3**, 161 (2011).

[19] H. Zhao, Y. Ma, Z. Gao, N. Liu, T. Wu, S. Wu, X. Feng, J. Hone, S. Strauf, and L. Feng, High-purity generation and switching of twisted single photons, Phys. Rev. Lett. **131**, 183801 (2023).

[20] G. C. G. Berkhout, M. P. J. Lavery, J. Courtial, M. W. Beijersbergen, and M. J. Padgett, Efficient sorting of orbital angular momentum states of light, Phys. Rev. Lett. **105**, 153601 (2010).

[21] H. Di Lorenzo Pires, H. C. B. Florijn, and M. P. van Exter, Measurement of the spiral spectrum of entangled two-photon states, Phys. Rev. Lett. **104**, 020505 (2010).

[22] E. Karimi, D. Giovannini, E. Bolduc, N. Bent, F. M. Miatto, M. J. Padgett, and R. W. Boyd, Exploring the quantum nature of the radial degree of freedom of a photon via Hong-Ou-Mandel interference, Phys. Rev. A **89**, 013829 (2014).

[23] Y. Zhou, M. Mirhosseini, D. Fu, J. Zhao, S. M. Hashemi Rafsanjani, A. E. Willner, and R. W. Boyd, Sorting photons by radial quantum number, Phys. Rev. Lett. **119**, 263602 (2017).

[24] D. Zia, N. Dehghan, A. D'Errico, F. Sciarrino, and E. Karimi, Interferometric imaging of amplitude and phase of spatial biphoton states, Nat. Photon. **17**, 1009 (2023).

[25] S. Karan, R. Prasad, and A. K. Jha, Postselection-free controlled generation of a high-dimensional orbital-angular-momentum entangled state, Phys. Rev. Appl. **20**, 054027 (2023).

[26] Ş. Suciu, G. A. Bulzan, T. A. Isdrailă, A. M. Pălici, S. Ataman, C. Kusko, and R. Ionicioiu, Quantum communication networks with optical vortices, Phys. Rev. A **108**, 052612 (2023).

[27] G. F. Quinteiro, D. E. Reiter, and T. Kuhn, Formulation of the twisted-light–matter interaction at the phase singularity: The twisted-light gauge, Phys. Rev. A **91**, 033808 (2015).

[28] G. F. Quinteiro, D. E. Reiter, and T. Kuhn, Formulation of the twisted-light–matter interaction at the phase singularity: Beams with strong magnetic fields, Phys. Rev. A **95**, 012106 (2017).

[29] S. Gao, F. C. Speirits, F. Castellucci, S. Franke-Arnold, S. M. Barnett, and J. B. Götte, Paraxial skyrmionic beams, Phys. Rev. A **102**, 053513 (2020).

[30] T. Zanon-Willette, F. Impens, E. Arimondo, D. Wilkowski, A. V. Taichenachev, and V. I. Yudin, Engineering quantum control with optical transitions induced by twisted light fields, Phys. Rev. A **108**, 043513 (2023).

[31] Z.-W. Lu, L. Guo, Z.-Z. Li, M. Ababekri, F.-Q. Chen, C. Fu, C. Lv, R. Xu, X. Kong, Y.-F. Niu, and J.-X. Li, Manipulation of giant multipole resonances via vortex γ photons, Phys. Rev. Lett. **131**, 202502 (2023).

[32] H. Kohl and H. Rose, in *Advances in Electronics and Electron Physics*, edited by P. W. Hawkes (Academic, New York, 1985) Vol. 65, pp. 173–227.

[33] D. A. Muller and J. Silcox, Delocalization in inelastic scattering, Ultramicroscopy **59**, 195 (1995).

[34] J. Yuan and N. K. Menon, Magnetic linear dichroism in electron energy loss spectroscopy, J. Appl. Phys. **81**, 5087 (1997).

[35] P. Schattschneider and W. S. M. Werner, Coherence in electron energy loss spectrometry, J. Electron Spectrosc. Relat. Phenom. **143**, 81 (2005).

[36] A. P. Hitchcock, Near edge electron energy loss spectroscopy: Comparison to x-ray absorption, Jpn. J. Appl. Phys. **32**, 176 (1993).

[37] C. Hébert and P. Schattschneider, A proposal for dichroic experiments in the electron microscope, Ultramicroscopy **96**, 463 (2003).

[38] P. Schattschneider, S. Rubino, C. Hébert, J. Rusz, J. Kuneš, P. Novák, E. Carlino, M. Fabrizioli, G. Panaccione, and G. Rossi, Detection of magnetic circular dichroism using a transmission electron microscope, Nature (London) **441**, 486 (2006).

[39] P. Schattschneider, B. Schaffer, I. Ennen, and J. Verbeeck, Mapping spin-polarized transitions with atomic resolution, Phys. Rev. B **85**, 134422 (2012).

[40] S. Muto, J. Rusz, K. Tatsumi, R. Adam, S. Arai, V. Kocevski, P. M. Oppeneer, D. E. Bürgler, and C. M. Schneider, Quantitative characterization of nanoscale polycrystalline magnets with electron magnetic circular dichroism, Nat. Commun. **5**, 3138 (2014).

[41] J. Rusz, J.-C. Idrobo, and S. Bhowmick, Achieving atomic resolution magnetic dichroism by controlling the phase symmetry of an electron probe, Phys. Rev. Lett. **113**, 145501 (2014).

[42] M. Xu, A. Li, S. J. Pennycook, S.-P. Gao, and W. Zhou, Probing a defect-site-specific electronic orbital in graphene with single-atom sensitivity, Phys. Rev. Lett. **131**, 186202 (2023).

[43] K. Müller, F. F. Krause, A. Béché, M. Schowalter, V. Galioit, S. Löffler, J. Verbeeck, J. Zweck, P. Schattschneider, and A. Rosenauer, Atomic electric fields revealed by a quantum mechanical approach to electron picodiffraction, Nat. Commun. **5**, 5653 (2014).

[44] M. C. Chirita Mihaila, P. Weber, M. Schneller, L. Grandits, S. Nimmrichter, and T. Juffmann, Transverse electron-beam shaping with light, Phys. Rev. X **12**, 031043 (2022).

[45] J. Verbeeck, H. Tian, and P. Schattschneider, Production and application of electron vortex beams, Nature (London) **467**, 301 (2010).

[46] B. J. McMorran, A. Agrawal, I. M. Anderson, A. A. Herzing, H. J. Lezec, J. J. McClelland, and J. Unguris, Electron vortex beams with high quanta of orbital angular momentum, Science **331**, 192 (2011).

[47] V. Grillo, G. C. Gazzadi, E. Mafakheri, S. Frabboni, E. Karimi, and R. W. Boyd, Holographic generation of highly twisted electron beams, Phys. Rev. Lett. **114**, 034801 (2015).

[48] M. Uchida and A. Tonomura, Generation of electron beams carrying orbital angular momentum, Nature (London) **464**, 737 (2010).

[49] G. M. Vanacore, G. Berruto, I. Madan, E. Pomarico, P. Biagioni, R. J. Lamb, D. McGrouther, O. Reinhardt, I. Kaminer, B. Barwick, H. Larocque, V. Grillo, E. Karimi, F. J. García de Abajo, and F. Carbone, Ultrafast generation and control of an electron vortex beam via chiral plasmonic near fields, Nat. Mater. **18**, 573 (2019).

[50] I. Madan, V. Leccese, A. Mazur, F. Barantani, T. LaGrange, A. Sapozhnik, P. M. Tengdin, S. Gargiulo, E. Rotunno, J.-C. Olaya, I. Kaminer, V. Grillo, F. J. García de Abajo, F. Carbone, and G. M. Vanacore, Ultrafast transverse modulation of free electrons by interaction with shaped optical fields, ACS Photonics **9**, 3215 (2022).

[51] F. J. García de Abajo, Optical excitations in electron microscopy, Rev. Mod. Phys. **82**, 209 (2010).

[52] K. Wang, R. Dahan, M. Shentcis, Y. Kauffmann, A. Ben Hayun, O. Reinhardt, S. Tsesses, and I. Kaminer, Coherent interaction between free electrons and a photonic cavity, Nature (London) **582**, 50 (2020).

[53] M. V. Tsarev, A. Ryabov, and P. Baum, Free-electron qubits and maximum-contrast attosecond pulses via temporal talbot revivals, Phys. Rev. Res. **3**, 043033 (2021).

[54] R. Dahan, G. Baranes, A. Gorlach, R. Ruimy, N. Rivera, and I. Kaminer, Creation of optical cat and GKP states using shaped free electrons, Phys. Rev. X **13**, 031001 (2023).

[55] T. Schachinger, P. Hartel, P.-H. Lu, S. Löffler, M. Obermair, M. Dries, D. Gerthsen, R. E. Dunin-Borkowski, and P. Schattschneider, Experimental realization of a $\pi/2$ vortex mode converter for electrons using a spherical aberration corrector, Ultramicroscopy **229**, 113340 (2021).

[56] S. Löffler, Unitary two-state quantum operators realized by quadrupole fields in the electron microscope, Ultramicroscopy **234**, 113456 (2022).

[57] S. Löffler, T. Schachinger, P. Hartel, P.-H. Lu, R. E. Dunin-Borkowski, M. Obermair, M. Dries, D. Gerthsen, and P. Schattschneider, A quantum logic gate for free electrons, Quantum **7**, 1050 (2023).

[58] A. H. Tavabi, P. Rosi, E. Rotunno, A. Roncaglia, L. Belsito, S. Frabboni, G. Pozzi, G. C. Gazzadi, P.-H. Lu, R. Nijland, M. Ghosh, P. Tiemeijer, E. Karimi, R. E. Dunin-Borkowski, and V. Grillo, Experimental demonstration of an electrostatic orbital angular momentum sorter for electron beams, Phys. Rev. Lett. **126**, 094802 (2021).

[59] A. Asenjo-Garcia and F. J. García de Abajo, Dichroism in the interaction between vortex electron beams, plasmons, and molecules, Phys. Rev. Lett. **113**, 066102 (2014).

[60] D. Ugarte and C. Ducati, Controlling multipolar surface plasmon excitation through the azimuthal phase structure of electron vortex beams, Phys. Rev. B **93**, 205418 (2016).

[61] G. Guzzinati, A. Béché, H. Lourenço-Martins, J. Martin, M. Kociak, and J. Verbeeck, Probing the symmetry of the

potential of localized surface plasmon resonances with phase-shaped electron beams, Nat. Commun. **8**, 14999 (2017).

[62] W. Cai, O. Reinhardt, I. Kaminer, and F. J. García de Abajo, Efficient orbital angular momentum transfer between plasmons and free electrons, Phys. Rev. B **98**, 045424 (2018).

[63] M. Zanfrognini, E. Rotunno, S. Frabboni, A. Sit, E. Karimi, U. Hohenester, and V. Grillo, Orbital angular momentum and energy loss characterization of plasmonic excitations in metallic nanostructures in TEM, ACS Photonics **6**, 620 (2019).

[64] N. Rivera, L. J. Wong, M. Soljačić, and I. Kaminer, Ultrafast multiharmonic plasmon generation by optically dressed electrons, Phys. Rev. Lett. **122**, 053901 (2019).

[65] H. Lourenço-Martins, D. Gérard, and M. Kociak, Optical polarization analogue in free electron beams, Nat. Phys. **17**, 598 (2021).

[66] M. R. Bourgeois, A. G. Nixon, M. Chalifour, E. K. Beutler, and D. J. Masiello, Polarization-resolved electron energy gain nanospectroscopy with phase-structured electron beams, Nano Lett. **22**, 7158 (2022).

[67] M. R. Bourgeois, A. G. Nixon, M. Chalifour, and D. J. Masiello, Optical polarization analogs in inelastic free-electron scattering, Sci. Adv. **9**, eadj6038 (2023).

[68] F. Aguilar, H. Lourenço-Martins, D. Montero, X. Li, M. Kociak, and A. Campos, Selective probing of longitudinal and transverse plasmon modes with electron phase-matching, J. Phys. Chem. C **127**, 22252 (2023).

[69] F. J. García de Abajo and M. Kociak, Probing the photonic local density of states with electron energy loss spectroscopy, Phys. Rev. Lett. **100**, 106804 (2008).

[70] F. J. García de Abajo and M. Kociak, Electron energy-gain spectroscopy, New J. Phys. **10**, 073035 (2008).

[71] A. Asenjo-Garcia and F. J. García de Abajo, Plasmon electron energy-gain spectroscopy, New J. Phys. **15**, 103021 (2013).

[72] C. Liu, Y. Wu, Z. Hu, J. A. Busche, E. K. Beutler, N. P. Montoni, T. M. Moore, G. A. Magel, J. P. Camden, D. J. Masiello, G. Duscher, and P. D. Rack, Continuous wave resonant photon stimulated electron energy-gain and electron energy-loss spectroscopy of individual plasmonic nanoparticles, ACS Photonics **6**, 2499 (2019).

[73] P. Das, J. D. Blazit, M. Tencé, L. F. Zagonel, Y. Auad, Y. H. Lee, X. Y. Ling, A. Losquin, C. Colliex, O. Stéphan, F. J. García de Abajo, and M. Kociak, Stimulated electron energy loss and gain in an electron microscope without a pulsed electron gun, Ultramicroscopy **203**, 44 (2019).

[74] M. R. Bourgeois, E. K. Beutler, S. Khorasani, N. Panek, and D. J. Masiello, Nanometer-scale spatial and spectral mapping of exciton polaritons in structured plasmonic cavities, Phys. Rev. Lett. **128**, 197401 (2022).

[75] R. J. Glauber and M. Lewenstein, Quantum optics of dielectric media, Phys. Rev. A **43**, 467 (1991).

[76] P. T. Kristensen, R.-C. Ge, and S. Hughes, Normalization of quasinormal modes in leaky optical cavities and plasmonic resonators, Phys. Rev. A **92**, 053810 (2015).

[77] R.-C. Ge and S. Hughes, Quasinormal mode theory and modelling of electron energy loss spectroscopy for plasmonic nanostructures, J. Opt. **18**, 054002 (2016).

[78] S. Franke, S. Hughes, M. K. Dezfouli, P. T. Kristensen, K. Busch, A. Knorr, and M. Richter, Quantization of quasinormal modes for open cavities and plasmonic cavity quantum electrodynamics, Phys. Rev. Lett. **122**, 213901 (2019).

[79] K. Y. Bliokh, P. Schattschneider, J. Verbeeck, and F. Nori, Electron vortex beams in a magnetic field: A new twist on Landau levels and Aharonov-Bohm states, Phys. Rev. X **2**, 041011 (2012).

[80] R. Van Boxem, B. Partoens, and J. Verbeeck, Rutherford scattering of electron vortices, Phys. Rev. A **89**, 032715 (2014).

[81] R. Van Boxem, B. Partoens, and J. Verbeeck, Inelastic electron-vortex-beam scattering, Phys. Rev. A **91**, 032703 (2015).

[82] V. Grillo, E. Karimi, G. C. Gazzadi, S. Frabboni, M. R. Dennis, and R. W. Boyd, Generation of nondiffracting electron Bessel beams, Phys. Rev. X **4**, 011013 (2014).

[83] K. Y. Bliokh, I. P. Ivanov, G. Guzzinati, L. Clark, R. Van Boxem, A. Béché, R. Juchtmans, M. A. Alonso, P. Schattschneider, F. Nori, and J. Verbeeck, Theory and applications of free-electron vortex states, Phys. Rep. **690**, 1 (2017).

[84] P. Schattschneider, M. Stöger-Pollach, and J. Verbeeck, Novel vortex generator and mode converter for electron beams, Phys. Rev. Lett. **109**, 084801 (2012).

[85] S. M. Lloyd, M. Babiker, G. Thirunavukkarasu, and J. Yuan, Electron vortices: Beams with orbital angular momentum, Rev. Mod. Phys. **89**, 035004 (2017).

[86] R. H. Ritchie, Plasma losses by fast electrons in thin films, Phys. Rev. **106**, 874 (1957).

[87] U. Hohenester, H. Ditlbacher, and J. R. Krenn, Electron-energy-loss spectra of plasmonic nanoparticles, Phys. Rev. Lett. **103**, 106801 (2009).

[88] F. J. García de Abajo and V. Di Giulio, Optical excitations with electron beams: Challenges and opportunities, ACS Photonics **8**, 945 (2021).

[89] P. Schattschneider, C. Hébert, H. Franco, and B. Jouffrey, Anisotropic relativistic cross sections for inelastic electron scattering, and the magic angle, Phys. Rev. B **72**, 045142 (2005).

[90] J. Sakurai and J. Napolitano, *Modern Quantum Mechanics*, 2nd ed. (Addison-Wesley, Reading, 2011).

[91] N. W. Bigelow, A. Vaschillo, V. Iberi, J. P. Camden, and D. J. Masiello, Characterization of the electron- and photon-driven plasmonic excitations of metal nanorods, ACS Nano **6**, 7497 (2012).

[92] N. W. Bigelow, A. Vaschillo, J. P. Camden, and D. J. Masiello, Signatures of Fano interferences in the electron energy loss spectroscopy and cathodoluminescence of symmetry-broken nanorod dimers, ACS Nano **7**, 4511 (2013).

[93] B. T. Draine and P. J. Flatau, Discrete-dipole approximation for periodic targets: Theory and tests, J. Opt. Soc. Am. A **25**, 2693 (2008).

[94] N. Talebi, W. Sigle, R. Vogelgesang, and P. van Aken, Numerical simulations of interference effects in photon-assisted electron energy-loss spectroscopy, New J. Phys. **15**, 053013 (2013).

[95] Y. Cao, A. Manjavacas, N. Large, and P. Nordlander, Electron energy-loss spectroscopy calculation in finite-difference time-domain package, ACS Photonics **2**, 369 (2015).

[96] U. Hohenester and A. Trügler, MNPBEM—A Matlab toolbox for the simulation of plasmonic nanoparticles, Comput. Phys. Commun. **183**, 370 (2012).

[97] H. Duan, A. I. Fernández-Domínguez, M. Bosman, S. A. Maier, and J. K. W. Yang, Nanoplasmonics: Classical down to the nanometer scale, Nano Lett. **12**, 1683 (2012).

[98] J. Pomplun, S. Burger, L. Zschiedrich, and F. Schmidt, Adaptive finite element method for simulation of optical nano structures, Phys. Status Solidi B **244**, 3419 (2007).

[99] E. M. Purcell and C. R. Pennypacker, Scattering and absorption of light by nonspherical dielectric grains, Astrophys. J. **186**, 705 (1973).

[100] P. B. Johnson and R. W. Christy, Optical constants of the noble metals, Phys. Rev. B **6**, 4370 (1972).

[101] R. Li, D. Wang, J. Guan, W. Wang, X. Ao, G. C. Schatz, R. Schaller, and T. W. Odom, Plasmon nanolasing with aluminum nanoparticle arrays, J. Opt. Soc. Am. B **36**, E104 (2019).

[102] C. Hébert, P. Schattschneider, H. Franco, and B. Jouffrey, ELNES at magic angle conditions, Ultramicroscopy **106**, 1139 (2006).

[103] X. Yin, M. Schäferling, B. Metzger, and H. Giessen, Interpreting chiral nanophotonic spectra: the plasmonic Born-Kuhn model, Nano Lett. **13**, 6238 (2013).

[104] T. Fu, T. Wang, Y. Chen, Y. Wang, Y. Qu, and Z. Zhang, Chiral near-fields around chiral dolmen nanostructure, J. Phys. D **50**, 474004 (2017).

[105] L. A. Warning, A. R. Miandashti, L. A. McCarthy, Q. Zhang, C. F. Landes, and S. Link, Nanophotonic approaches for chirality sensing, ACS Nano **15**, 15538 (2021).

[106] T. R Harvey, J. S Pierce, A. K Agrawal, P. Ercius, M. Linck, and B. J. McMorran, Efficient diffractive phase optics for electrons, New J. Phys. **16**, 093039 (2014).

[107] F. S. Yasin, T. R. Harvey, J. J. Chess, J. S. Pierce, C. Ophus, P. Ercius, and B. J. McMorran, Probing light atoms at subnanometer resolution: Realization of scanning transmission electron microscope holography, Nano Lett. **18**, 7118 (2018).

[108] H. Lourenço-Martins, A. Lubk, and M. Kociak, Bridging nano-optics and condensed matter formalisms in a unified description of inelastic scattering of relativistic electron beams, SciPost Phys. **10**, 031 (2021).

[109] A. B. Hayun, O. Reinhardt, J. Nemirovsky, A. Karnieli, N. Rivera, and I. Kaminer, Shaping quantum photonic states using free electrons, Sci. Adv. **7**, eabe4270 (2021).

[110] T. J. Davis, D. Janoschka, P. Dreher, B. Frank, F. J. Meyer zu Heringdorf, and H. Giessen, Ultrafast vector imaging of plasmonic skyrmion dynamics with deep subwavelength resolution, Science **368**, eaba6415 (2020).

[111] Y. Shen, E. C. Martínez, and C. Rosales-Guzmán, Generation of optical skyrmions with tunable topological textures, ACS Photonics **9**, 296 (2022).

[112] L. Gao, S. Prokhorenko, Y. Nahas, and L. Bellaiche, Dynamical multiferroicity and magnetic topological structures induced by the orbital angular momentum of light in a nonmagnetic material, Phys. Rev. Lett. **131**, 196801 (2023).

[113] A. Ghosh, S. Yang, Y. Dai, and H. Petek, The spin texture topology of polygonal plasmon fields, ACS Photonics **10**, 13 (2023).